

Symmetry Energy Constraints from Giant Resonances: A Theoretical Overview

J. Piekarewicz

Department of Physics
Florida State University
Tallahassee, FL 32306-4350
USA

Received: date / Revised version: date

Abstract. Giant resonances encapsulate the dynamic response of the nuclear ground state to external perturbations. As such, they offer a unique view of the nucleus that is often not accessible otherwise. Although interesting in their own right, giant resonances are also enormously valuable in providing stringent constraints on the equation of state of asymmetric matter. We take this view in mind, we focus on two modes of excitation that are essential in reaching this goal: the isoscalar giant monopole resonance (GMR) and the isovector giant dipole resonance (GDR). GMR energies in heavy nuclei are sensitive to the symmetry energy because they probe the incompressibility of neutron-rich matter. Unfortunately, access to the symmetry energy is hindered by the relatively low neutron-proton asymmetry of stable nuclei. Thus, the measurement of GMR energies in exotic nuclei is strongly encouraged. In the case of the GDR, we find the electric dipole polarizability of paramount importance. Indeed, the electric dipole polarizability appears as one of two laboratory observables—with the neutron-skin thickness being the other—that are highly sensitive to the density dependence of the symmetry energy. Finally, we identify the softness of skin and the nature of the pygmy resonance as important unsolved problems in nuclear structure.

PACS. 21.65.Ef Symmetry energy – 24.30.Cz Giant resonances – 21.60.Jz Nuclear Density Functional Theory – 24.10.Jv Relativistic models

1 Introduction

Nuclear saturation, the existence of an equilibrium density, is a hallmark of the nuclear dynamics. That the size of the nucleus increases as $A^{1/3}$ is one of the best-known consequences of nuclear saturation. The venerable semi-empirical mass formula of Bethe and Weizsäcker, conceived shortly after the discovery of the neutron by Chadwick, treats the nucleus as an incompressible quantum drop consisting of Z protons and N neutrons ($A=Z+N$). The mass formula may be written in general in terms of the individual nucleon masses (m_p and m_n) and the nuclear binding energy $B(Z, N)$ that contains all the complicated nuclear dynamics: $M(Z, N) = Zm_p + Nm_n - B(Z, N)$. In the context of the liquid-drop formula the binding energy is written in terms of a handful of empirical parameters that portray the physics of a quantum drop. That is,

$$B(Z, N) = a_v A - a_s A^{2/3} - a_c \frac{Z^2}{A^{1/3}} - a_a \frac{(N-Z)^2}{A} + \dots \quad (1)$$

The volume term represents the binding energy of a large and symmetric ($Z=N=A/2 \gg 1$) system in the absence of Coulomb forces. The next three terms are correction terms

due to the development of a nuclear surface, the Coulomb repulsion among protons, and the Pauli exclusion principle that favors symmetric systems. Note that in both the surface and Coulomb terms one has already used nuclear saturation to write the radius of the nucleus in terms of the equilibrium (or saturation) density $\rho_0 = 0.148 \text{ fm}^{-3}$ as follows:

$$R(A) = r_0 A^{1/3}, \quad \text{where } r_0 = \sqrt[3]{\frac{3}{4\pi\rho_0}} = 1.17 \text{ fm}. \quad (2)$$

Although such a smooth formula gives a remarkably good description of the masses of stable nuclei, it is unable to account for local fluctuations associated with the emergence of nuclear shells and the concomitant appearance of magic numbers. To overcome such a drawback, a *macroscopic-microscopic* approach was developed, where the nuclear binding energy is separated into two components: one large and smooth (as in the liquid drop model) and the other one small and fluctuating to properly account for shell effects. The macroscopic-microscopic approach has enjoyed its greatest success in the work of Möller and collaborators [1, 2, 3], and Dufo and Zuker [4, 5, 6]. Although refinements to the mass formula have been made to meet new

and increasing challenges, the structure of this 75 year-old formula remains practically unchanged.

We now consider the thermodynamic limit of the liquid-drop formula in which both the number of nucleons and the volume are taken to infinity, but their ratio remains fixed at the saturation density. Moreover, we ignore the electroweak sector so that Coulomb forces are absent and both Z and N are individually conserved. In this limit the binding energy per nucleon may be written as

$$\mathcal{E}(\alpha) \equiv -\frac{B(Z, N)}{A} = \varepsilon_0 + J\alpha^2, \quad (3)$$

where $\varepsilon_0 = -a_v$, $J = a_a$, and $\alpha = (N - Z)/A$ is the neutron-proton asymmetry. This simple formula suggests that a large symmetric liquid drop of density ρ_0 has a binding energy per nucleon of $\varepsilon_0 \approx -16$ MeV and that there is an energy cost of $J \approx 32$ MeV in converting all protons into neutrons, namely, in turning symmetric nuclear matter into pure neutron matter. However, in reality the liquid drop is not incompressible, so the semi-empirical mass formula fails to capture the response of the liquid drop to density fluctuations. Given that the liquid-drop formula provides a remarkably good description of the masses of stable nuclei, it is evident that nuclear masses alone, while highly sensitive to ε_0 and J , are insensitive to the density dependence of these parameters. Note that the equation of state (EOS) $E(\rho, \alpha)$ dictates how the energy per nucleon changes as a function of both the density and the neutron-proton asymmetry. In essence then, the masses of stable nuclei provide meaningful constraints only for $E(\rho \approx \rho_0, \alpha)$.

To probe the density dependence of the EOS one must study the response of the liquid drop to external perturbations. That is, one uses an external probe to drive the system away from equilibrium and then records how the system responds to such a perturbation. In this contribution we will focus on two particular nuclear excitation modes: the isoscalar monopole resonance and the isovector dipole resonance [7]. For the impact of other excitation modes in constraining the nuclear equation of state see Refs. [8, 9, 10], references contained therein, and the contribution to this volume by Colò, Garg, and Sagawa.

The isoscalar monopole resonance measures the collective response of the nucleus to density fluctuations. Pictorially, this collective excitation in which protons and neutrons oscillate in phase around the equilibrium density may be perceived as a spherical *breathing* mode. Given that nuclear matter saturates, the pressure at saturation density vanishes. Thus, the isoscalar monopole resonance probes the curvature of the EOS at saturation density, or equivalently, the incompressibility of neutron-rich matter [11]. Naturally, the incompressibility of asymmetric matter is sensitive to the symmetry energy. However, a more direct probe of the density dependence of the symmetry energy is the isovector dipole resonance. One may visualize this mode of excitation as an out of phase displacement of neutrons relative to protons. Given that this oscillation results in the formation of two dilute quantum fluids—one neutron rich and the other one proton rich—the symmetry energy acts as the restoring force. Note that in contrast

to the EOS of symmetric nuclear matter, the symmetry pressure does not vanish at saturation density. An enormous effort has been devoted in recent years to determine the symmetry pressure.

Even though our contribution to this special volume is limited to giant resonances, we find useful to discuss briefly the impact of other observables in constraining the nuclear symmetry energy. Although the symmetry pressure (or equivalently the slope of the symmetry energy at saturation density L) is not an observable, it has been shown to be strongly correlated to the neutron-skin thickness of ^{208}Pb [12, 13, 14, 15]. The neutron-skin thickness is defined as the difference between the neutron (r_n) and proton (r_p) root-mean-square radii. The charge (and proton) distribution in nuclei is known with exquisite accuracy due to the pioneering work of Hofstadter in the late 1950's [16] and that continues to this day with the advent of powerful continuous electron beam facilities. Instead, challenging parity-violating experiments are required to cleanly measure neutron densities [17]. Indeed, because the weak charge of the neutron is much larger than that of the proton, parity-violating electron scattering provides a clean probe of the neutron radius that is free from large and uncontrolled strong-interaction uncertainties. As one combines these results with the highly-precise measurements of nuclear charge radii [18], one obtains a fairly model-independent determination of the neutron-skin thickness of ^{208}Pb , and thus a stringent constraint on the density dependence of the symmetry energy. We note that the Lead Radius Experiment (“PREX”) at the Jefferson Laboratory has provided the first model-independent evidence on the existence of a neutron-rich skin in ^{208}Pb [19, 20]. Through the use of some mild assumptions PREX determined the neutron-skin of ^{208}Pb to be [19]:

$$r_{\text{skin}}^{208} \equiv r_n^{208} - r_p^{208} = 0.33_{-0.18}^{+0.16} \text{ fm}. \quad (4)$$

For a detailed account of this significant achievement and efforts to measure the neutron-skin thickness of ^{48}Ca , see the contribution to this volume by Horowitz, Kumar, and Michaels. An accurate determination of the neutron radius of ^{208}Pb —and the resulting constrain on L —represents a critical milestone with far reaching implications in areas as diverse as nuclear structure [12, 13, 14, 15], atomic parity violation [21, 22, 23, 24], heavy-ion collisions [25, 26, 27, 28, 29], and neutron-star structure [30, 31, 32, 33, 34, 35, 36, 37]. Conversely, due to major advances in all these areas significant constraints on L are starting to emerge as one combines theoretical, experimental, and observational information [38, 39, 40, 41, 42, 43, 44]. It is the aim of this special volume to summarize the successes of the past and the challenges of the future in understanding the density dependence of the symmetry energy. In particular, this review contributes to this common goal by using powerful insights from nuclear collective excitations.

The manuscript has been organized as follows. In Sec. 2 we review the relativistic random phase approximation (RPA) formalism required to compute the distribution of isoscalar monopole and isovector dipole strength. Particular emphasis is placed on the role of these resonances in

constraining the density dependence of the symmetry energy. In Sec. 3 we present results from a variety of nuclear energy density functionals (EDFs) and highlight the impact of these collective modes in constraining these models. Finally, we offer our conclusions and summarize the challenges for the future in Sec. 4.

2 Formalism

This section is subdivided into three subsections. In the first subsection we introduce the relativistic formalism required to compute the distribution of both monopole and dipole strength. Then, we proceed to discuss the merits of the distribution of isoscalar monopole strength, particularly in neutron-rich nuclei, in constraining simultaneously the incompressibility coefficient of symmetric nuclear matter and the density dependence of the symmetry energy. Finally, the last subsection is reserved to a discussion of the isovector dipole resonance. In particular, we identify the electric dipole polarizability as a strong isovector indicator.

2.1 Relativistic Density Functional Theory

Historically, relativistic models of nuclear structure were strictly limited to renormalizable field theories [45, 46]. The appeal of renormalizability was that a handful of model parameters could be calibrated to well-known physical observables so that one could then later extrapolate to unknown physical regions without the need for introducing additional parameters. However, the modern viewpoint suggests that these relativistic models should be treated as effective field theories (EFTs) where the demand for renormalizability is no longer required. Yet, EFTs should continue to provide a consistent framework for the nuclear many-body problem [47]. An effective field theory is designed to describe low-energy physics without any attempt at accounting for its detailed short-distance behavior. By calibrating the model directly to physical observables, the short-distance structure of the theory, as well as other complicated many-body effects, gets implicitly encoded in the parameters of the model. In this regard, density functional theory (DFT) provides a powerful framework for the construction of an effective field theory [48, 49, 50]. A meaningful criterion used to construct the relativistic density functional was proposed by Furnstahl and collaborators based on the concept of “*naive dimensional analysis*” and “*naturalness*” [51, 52, 53, 54, 55]. Such an approach is both useful and powerful as it allows an organizational scheme based on an expansion in powers of the meson fields; terms in the effective Lagrangian with a large number of meson fields are suppressed by a large mass scale. In principle then, all terms to a given order must be retained. In practice, however, many of these terms have been ignored. The “justification” behind these fairly ad-hoc procedure is that whereas the neglected terms are of the same order in a power-counting scheme, the full

set of parameters is poorly constrained by existing experimental data. Thus, ignoring a subset of these terms does not compromise the quality of the fit [51, 56].

2.1.1 Relativistic Lagrangian

The starting point for the relativistic calculation of the nuclear response is the interacting Lagrangian density of Ref. [56] supplemented by an isoscalar-isovector term originally introduced in Ref. [30]. That is,

$$\begin{aligned} \mathcal{L}_{\text{int}} = & \bar{\psi} \left[g_s \phi - \left(g_v V_\mu + \frac{g_\rho}{2} \boldsymbol{\tau} \cdot \mathbf{b}_\mu + \frac{e}{2} (1 + \tau_3) A_\mu \right) \gamma^\mu \right] \psi \\ & - \frac{\kappa}{3!} (g_s \phi)^3 - \frac{\lambda}{4!} (g_s \phi)^4 + \frac{\zeta}{4!} g_v^4 (V_\mu V^\mu)^2 \\ & + \Lambda_v \left(g_\rho^2 \mathbf{b}_\mu \cdot \mathbf{b}^\mu \right) \left(g_v^2 V_\nu V^\nu \right). \end{aligned} \quad (5)$$

Motivated by a desire to provide a Lorentz covariant extrapolation to dense neutron-star matter, Walecka introduced a Lagrangian density with an isodoublet nucleon field ψ interacting through the exchange of two massive isoscalar “mesons”: a scalar ϕ and a vector V^μ [45]. Remarkably, such a simple model was already able to account for nuclear saturation at the mean-field level. Although the two parameters of the model (g_s and g_v) were adjusted to reproduce the density and binding energy at saturation, the saturation mechanism was identified as being of relativistic origin. Indeed, whereas the vector repulsion continues to increase with baryon density, the scalar attraction, which is proportional to the “Lorentz contracted” scalar density, saturates. Moreover, to properly describe the equilibrium density and binding energy, both the scalar and vector mean fields were found to be very large (of about half of the nucleon rest mass). We note that large and canceling scalar and vector fields are the hallmark of the relativistic mean-field (RMF) theory. We also note that the pseudoscalar pion does not contribute at the mean-field level for a ground state of definite parity.

In order to move beyond infinite nuclear matter and to be able to describe the properties of finite nuclei, an isovector meson field (b^μ) and the photon (A^μ) were introduced. Relativistic mean-field equations for spherical nuclei were then solved self-consistently and a comparison against experiment revealed a level of agreement equivalent to that of the most sophisticated non-relativistic calculations available at the time [57, 58]. In particular, a non-relativistic reduction of the mean-field equations leads to a Schrödinger-like equation with unique central and spin-orbit potentials. Whereas the central potential displays the characteristic cancelation between the strong scalar and vector potentials, the strong potentials contribute coherently to the spin-orbit potential. Thus, the simple RMF approach was successful in accounting for both the relatively weak binding energy and strong spin-orbit splitting displayed by the single-particle spectrum.

In spite of the enormous success of the early RMF models, they all suffered from a major shortcoming: the incompressibility coefficient of symmetric nuclear matter

was predicted to be $K_0 \approx 550$ MeV. This was recognized early on to be excessively large. Hence, in an effort to overcome this deficiency, Boguta and Bodmer introduced cubic and quartic scalar meson self-interactions [59]. In particular, these terms (denoted by κ and λ) may be adjusted in such a way as to make the incompressibility coefficient of symmetric nuclear matter consistent with measurements of the distribution of isoscalar monopole strength in medium to heavy nuclei [60, 61, 62, 63, 64, 65, 66]. In fact, one may select suitable values for ρ_0 , ε_0 , K_0 , and M^* (with the latter denoting the effective nucleon mass at saturation density) and then obtain four of the isoscalar parameters of the model (g_s , g_v , κ and λ) by simply solving a set of four linear simultaneous equations [67]. Later on, two more parameters were introduced to soften the EOS. In the case of the isoscalar sector, omega-meson self-interactions (as described by the parameter ζ) serve to soften the equation of state of symmetric nuclear at high densities. Indeed, Müller and Serot found possible to build models with different values of ζ that reproduced the same observed nuclear properties at normal densities but which yield maximum neutron star masses that differ by almost one solar mass [56]. Such a finding suggests that observations of massive neutron stars [68, 69]—rather than laboratory experiment—may provide the only meaningful constraint on the high-density component of the EOS. Finally, A_v was introduced to modify the poorly constrained density dependence of the symmetry energy, while leaving the isoscalar sector intact [30, 31]. Doing so has served to uncover powerful correlations between the slope of the symmetry energy L and a host of both laboratory and astrophysical observables.

2.1.2 Relativistic Random Phase Approximation

Having defined the relativistic density functional one can now proceed to compute the linear response of the system to an external perturbation. The first step in a consistent mean-field plus RPA (MF+RPA) approach to the nuclear response is the calculation of various ground-state properties. This procedure is implemented by solving the equations of motion associated with the above Lagrangian density in a self-consistent, mean-field approximation [58]. For the various meson fields the mean-field approximation consists in solving (non-linear) Klein-Gordon equations with the appropriate baryon densities appearing as source terms. These baryon densities are computed from the nucleon orbitals that are, in turn, obtained from solving the one-body Dirac equation in the presence of scalar and time-like vector potentials—which themselves are written in terms of the various meson fields. This procedure must then be repeated until self-consistency is achieved. What emerges from such a self-consistent calculation is a set of single-particle energies and corresponding set of Dirac orbitals, and the self-consistently determined scalar and vector mean-field potentials. A detailed implementation of the mean-field procedure may be found in Ref. [70].

To compute the distribution of both monopole and dipole strength it is sufficient to concentrate on the longi-

tudinal nuclear response that is defined as

$$S(q, \omega) = \sum_n \left| \langle \Psi_n | \hat{\rho}(\mathbf{q}) | \Psi_0 \rangle \right|^2 \delta(\omega - \omega_n) = -\frac{1}{\pi} \Im \Pi(\mathbf{q}, \mathbf{q}; \omega), \quad (6)$$

where Ψ_0 is the exact nuclear ground state, Ψ_n is an excited state with excitation energy $\omega_n = E_n - E_0$, $\hat{\rho}(\mathbf{q})$ is the transition operator, and $\Pi(\mathbf{q}, \mathbf{q}; \omega)$ the associated polarization tensor. The transition operator is the Fourier transform of the vector density and it takes the following form:

$$\hat{\rho}_a(\mathbf{q}) = \int d^3r \bar{\psi}(\mathbf{r}) e^{-i\mathbf{q}\cdot\mathbf{r}} \gamma^0 \tau_a \psi(\mathbf{r}). \quad (7)$$

Here $\gamma^0 = \text{diag}(1, 1, -1, -1)$ is the zeroth component of the Dirac matrices, τ_0 is the identity matrix in isospin space, and $\tau_3 = \text{diag}(1, -1)$ is the third isospin matrix. The cornerstone of our theoretical approach is the polarization tensor defined in terms of a time-ordered product of two vector densities. That is,

$$i\Pi_{ab}(x, y) = \langle \Psi_0 | T \left[\hat{\rho}_a(x) \hat{\rho}_b(y) \right] | \Psi_0 \rangle \quad (8)$$

$$= \int_{-\infty}^{\infty} \frac{d\omega}{2\pi} e^{-i\omega(x^0 - y^0)} \Pi_{ab}(\mathbf{x}, \mathbf{y}; \omega). \quad (9)$$

Connecting the nuclear response to the polarization tensor is highly appealing as one can bring to bear the full power of the many-body formalism into the calculation of an experimental observable [71, 72]. In particular, the polarization tensor contains all dynamical information related to the excitation spectrum of the system. Moreover, the spectral content of the polarization tensor is both simple and illuminating: $\Pi_{ab}(\mathbf{x}, \mathbf{y}; \omega)$ is an analytic function of ω —except for simple poles located at the excitation energies and with the transition form-factors extracted from the residue at the corresponding pole.

The calculation of the nuclear response at the RPA level has the uncorrelated (or mean-field) polarization tensor as one of its main ingredients. In a mean-field approximation, the polarization tensor may be written exclusively in terms of the nucleon mean-field propagator G_F . That is,

$$\begin{aligned} \Pi_{ab}(\mathbf{x}, \mathbf{y}; \omega) = & \sum_{0 < n < F} \bar{U}_n(\mathbf{x}) \gamma^0 \tau_a G_F(\mathbf{x}, \mathbf{y}; +\omega + E_n^{(+)}) \gamma^0 \tau_b U_n(\mathbf{y}) + \\ & \sum_{0 < n < F} \bar{U}_n(\mathbf{y}) \gamma^0 \tau_b G_F(\mathbf{y}, \mathbf{x}; -\omega + E_n^{(+)}) \gamma^0 \tau_a U_n(\mathbf{x}), \end{aligned} \quad (10)$$

where $U_n(\mathbf{x})$ and $E_n^{(+)}$ are single-particle orbitals and energies determined from the self-consistent procedure, and the sum is limited to occupied positive-energy orbitals (i.e., below the Fermi surface). The Feynman mean-field propagator admits a spectral decomposition in terms of

the mean-field solutions to the Dirac equation, namely,

$$G_F(\mathbf{x}, \mathbf{y}; \omega) = \sum_n \left[\frac{U_n(\mathbf{x})\bar{U}_n(\mathbf{y})}{\omega - E_n^{(+)} + i\eta} + \frac{V_n(\mathbf{x})\bar{V}_n(\mathbf{y})}{\omega + E_n^{(-)} - i\eta} \right]. \quad (11)$$

Here U_n and V_n are the positive- and negative-energy solutions to the Dirac equation with the sum now over all states in the spectrum. Self-consistency demands that the nucleon propagator must satisfy an inhomogeneous Dirac equation with a mean-field potential identical to the one used to generate the ground state. Only then can fundamental symmetries be maintained, such as the conservation of the vector current and the decoupling of the spurious state from the RPA response.

As alluded earlier, the analytic structure of the polarization tensor provides critical insights. Indeed, the polarization tensor is an analytic function of ω , except for simple poles at $\omega = E_n^{(+)} - E_m^{(+)} > 0$, where $E_n^{(+)}$ ($E_m^{(+)}$) is a positive-energy orbital above (below) the Fermi surface. Moreover, the corresponding residues at the pole yield the transition form factors. Finally, note that the contribution from the negative-energy orbitals is purely real, as it is free of singularities for $\omega > 0$. This implies that negative-energy states make no contribution to the mean-field response. However, they play an essential role in the RPA response—as they are instrumental in ensuring current conservation and the decoupling of the spurious state [73]. Thus, in addition to the conventional particle-hole excitations, consistency demands the inclusion of pairs formed from occupied positive- and negative-energy states. Note that by themselves, the positive-energy states are not complete. We display in Fig. 1 the singularity structure of the nucleon propagator at finite density.

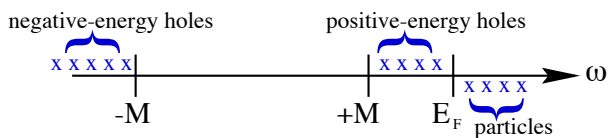


Fig. 1. (Color online) Analytic structure of the mean-field nucleon propagator. The propagator has singularities at the corresponding mean-field energies. For occupied orbitals—including the negative-energy sea—the singularities are located above the real axis; for empty states above the Fermi surface they are located below. In addition to the conventional particle-hole excitations, consistency demands transitions involving negative-energy states and occupied positive-energy orbitals [73].

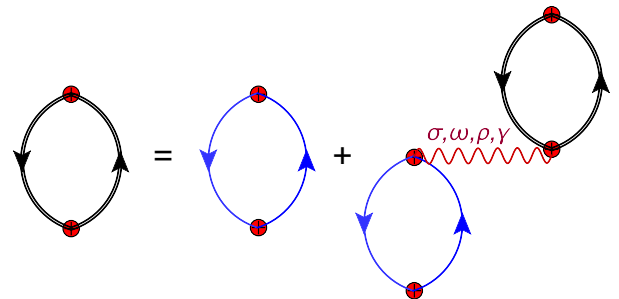
Although a spectral approach provides valuable physical insights, a scheme that efficiently incorporates all the required symmetries—while avoiding any reliance on artificial cut-offs and truncations—is the nonspectral approach [74, 75]. A nonspectral approach has the virtue that both positive- and negative-energy states (bound and continuum) are treated on equal footing. In this way the continuum width is treated exactly in the model. Thus, to obtain the mean-field propagator in nonspectral form one must solve the Green’s problem for the Dirac equation in the presence of a mean-field potential identical to the one used to generate the mean-field ground state.

Having generated the lowest-order (mean-field) polarization one may now proceed to compute the fully correlated RPA response. One goes beyond the single-particle response by building collectivity into the nuclear response through the mixing of many particle-hole excitations. This procedure is implemented by iterating the lowest-order polarization to all orders; see Fig. 2 for a diagrammatic representation. Given that the iteration is to all orders, the analytic structure of the propagator—and thus the location of the singularities—is modified relative to the lowest-order predictions. If many pairs are involved, then the nuclear response is strongly collective and one “giant resonance” dominates, namely, it exhausts most of the classical sum rule. Such an iterative procedure yields Dyson’s equation for the RPA polarization whose solution embodies the collective response of the ground state [71, 72]. That is,

$$\Pi_{ab}^{\text{RPA}}(\mathbf{q}, \mathbf{q}'; \omega) = \Pi_{ab}(\mathbf{q}, \mathbf{q}'; \omega) + \int \frac{d^3k}{(2\pi)^3} \frac{d^3k'}{(2\pi)^3} \Pi_{ac}(\mathbf{q}, \mathbf{k}; \omega) V_{cd}(\mathbf{k}, \mathbf{k}'; \omega) \Pi_{db}^{\text{RPA}}(\mathbf{k}', \mathbf{q}'; \omega), \quad (12)$$

where $V_{cd}(\mathbf{k}, \mathbf{k}'; \omega)$ is the residual interaction (see below) and $\Pi_{ab}(\mathbf{q}, \mathbf{q}'; \omega)$ is the Fourier transform of the lowest-order polarization:

$$\Pi_{ab}(\mathbf{q}, \mathbf{q}'; \omega) = \int d^3x d^3y e^{-i(\mathbf{q}\cdot\mathbf{x} - \mathbf{q}'\cdot\mathbf{y})} \Pi_{ab}(\mathbf{x}, \mathbf{y}; \omega). \quad (13)$$



$$\Pi_{\text{RPA}} = \Pi_0 + \Pi_0 V \Pi_{\text{RPA}}$$

Fig. 2. (Color online) Diagrammatic representation of the RPA equations. The ring with the thick black lines represents the fully correlated RPA polarization while the one depicted with the thin blue lines is the uncorrelated (mean-field) polarization. The residual interaction denoted with the red wavy line is identical to the one used to generate the mean-field ground state.

The computational demands imposed on relativistic RPA calculations are enormous. Powerful symmetries that were present in infinite nuclear matter, such as translational invariance, are now broken in the finite system. As a result, the RPA equations that were algebraic in the infinite system become integral equations in the finite nucleus. Moreover, modes of excitation that were uncoupled before (such as longitudinal-transverse or isoscalar-isovector) become coupled in the finite system. Indeed, for

nuclei with large neutron excess, the mixing of isoscalar and isovector modes is strong. Further, because of the ubiquitous meson mixing in relativistic theories (for example, scalar-vector mixing) the RPA equations become a complicated set of 9×9 coupled integral equations (1 involving ϕ , 4 involving V^μ , and 4 involving b_3^μ ; the photon, being “half isoscalar and half isovector”, may be absorbed into the last two terms). Finally, note that because of meson self-interactions, their respective propagators are no longer local in momentum space and depart from their simple Yukawa form. For example, the scalar propagator, given by $V_{ss}(\mathbf{x}, \mathbf{y}; \omega) = g_s^2 \Delta_s(\mathbf{x}, \mathbf{y}; \omega)$, satisfies the following complicated Klein-Gordon equation [75, 76]:

$$\left(\omega^2 + \nabla^2 - m_s^2 - \kappa\phi - \frac{1}{2}\lambda\phi^2\right)\Delta_s(\mathbf{x}, \mathbf{y}; \omega) = \delta(\mathbf{x} - \mathbf{y}). \quad (14)$$

Finally, with the mean-field polarization tensor Π_{ab} and the residual interaction V_{ab} at hand, one can now solve Dyson’s equation for the RPA polarization tensor using matrix inversion techniques. Note that whereas excitation modes become coupled in the finite system, the total angular momentum J and parity π remain good quantum numbers. Thus, the polarization tensor is decomposed into its various J^π components and one solves the RPA equations for only the channels of interest; $J^\pi = 0^+$ and $J^\pi = 1^-$ in our particular case.

2.2 Isoscalar Giant Monopole Resonance

We start this section by relaxing the early assumption of an incompressible liquid drop to allow for density fluctuations around the equilibrium density. In general, the energy per particle of asymmetric nuclear matter—at zero temperature and relative to the nucleon mass M —may be written as follows:

$$\frac{E}{A}(\rho, \alpha) - M \equiv \mathcal{E}(\rho, \alpha) = \mathcal{E}_{\text{SNM}}(\rho) + \alpha^2 \mathcal{S}(\rho) + \mathcal{O}(\alpha^4). \quad (15)$$

Given that the neutron-proton asymmetry is constrained to the interval $0 \leq \alpha \leq 1$, the total energy per particle $\mathcal{E}(\rho, \alpha)$ is customarily expanded in a power series in α^2 . Note that no odd powers of α appear as the nuclear force is isospin symmetric. The leading term in this expansion $\mathcal{E}_{\text{SNM}}(\rho)$ represents the energy of symmetric nuclear matter. In turn, the first-order correction to the symmetric limit is the symmetry energy $\mathcal{S}(\rho)$. To a very good approximation, the symmetry energy measures the energy cost in converting symmetric nuclear matter into pure neutron matter. That is,

$$\mathcal{S}(\rho) \approx \mathcal{E}(\rho, \alpha = 1) - \mathcal{E}(\rho, \alpha = 0). \quad (16)$$

In spite of the enormous progress made over the last years in measuring the masses of exotic nuclei [77], gaining access to the symmetry energy is hindered by the small α^2 prefactor. For example, even for ^{132}Sn —a nucleus with a significant neutron excess—the neutron-proton asymmetry amounts to only $\alpha^2 = (0.242)^2 = 0.059$. And whereas

nuclear masses have been measured accurately enough to provide valuable constraints on the symmetry energy at a density of $\rho \approx 0.1 \text{ fm}^{-3}$, its density dependence remains largely undetermined [13].

However, the response of the nuclear ground-state to density fluctuations is sensitive to the density dependence of the symmetry energy. To elucidate this fact, we expand both the energy of symmetric nuclear matter and the symmetry energy around the equilibrium density. That is [11],

$$\mathcal{E}_{\text{SNM}}(\rho) = \varepsilon_0 + \frac{1}{2}K_0x^2 + \frac{1}{6}Q_0x^3 + \dots \quad (17a)$$

$$\mathcal{S}(\rho) = J + Lx + \frac{1}{2}K_{\text{sym}}x^2 + \frac{1}{6}Q_{\text{sym}}x^3 + \dots \quad (17b)$$

where $x = (\rho - \rho_0)/3\rho_0$ is a dimensionless parameter that quantifies the deviations of the density from its value at saturation. Moreover, K_0 and Q_0 are the incompressibility coefficient and skewness parameter of symmetric nuclear matter; K_{sym} and Q_{sym} are the corresponding quantities for the symmetry energy. Note that unlike symmetric nuclear matter, the linear term in x (namely L) does not vanish in the case of the symmetry energy. By relying on these expansions, the energy per particle of asymmetric nuclear matter may be written in the following form [c.f. to Eq. (3)]:

$$\begin{aligned} \mathcal{E}(\rho, \alpha) = & (\varepsilon_0 + J\alpha^2) + L\alpha^2x + \frac{1}{2}(K_0 + \alpha^2K_{\text{sym}})x^2 \\ & + \frac{1}{6}(Q_0 + \alpha^2Q_{\text{sym}})x^3 + \dots \end{aligned} \quad (18)$$

Since the density pressure L does not vanish, the saturation point in asymmetric matter shifts from $x_0 = 0$ to \bar{x}_0 , where the latter is defined as the solution to $\partial\mathcal{E}/\partial x = 0$. To $\mathcal{O}(\alpha^2)$, the solution to this equation is simple and results in a shift of the saturation density to [11]:

$$\bar{x}_0 = -\frac{L}{K_0}\alpha^2 \implies \frac{\bar{\rho}_0}{\rho_0} = 1 + 3\bar{x}_0 = 1 - 3\frac{L}{K_0}\alpha^2. \quad (19)$$

Given that PREX has established the existence of a neutron rich skin in ^{208}Pb , the symmetry pressure must be positive, indicating that the saturation point must move to lower densities. In turn, the incompressibility coefficient of neutron-rich matter may now be found by expanding Eq. (18) around \bar{x}_0 . That is,

$$\mathcal{E}(\rho, \alpha) = \mathcal{E}(\bar{x}_0, \alpha) + \frac{1}{2}(x - \bar{x}_0)^2 \left(\frac{\partial^2 \mathcal{E}}{\partial x^2}\right)_{\bar{x}_0} + \dots \quad (20)$$

Alternatively, by introducing $\bar{x} = (\rho - \bar{\rho}_0)/3\bar{\rho}_0$ to quantify deviations from the new equilibrium density, we obtain in analogy to the symmetric case, the following expression:

$$\mathcal{E}(\rho, \alpha) = (\varepsilon_0 + J\alpha^2) + \frac{1}{2}K_0(\alpha)\bar{x}^2 + \dots \quad (21)$$

where the incompressibility coefficient of neutron-rich matter is given to $\mathcal{O}(\alpha^2)$ by [11]

$$K_0(\alpha) = K_0 + K_\tau\alpha^2 \equiv K_0 + \left(K_{\text{sym}} - 6L - \frac{Q_0}{K_0}L\right)\alpha^2. \quad (22)$$

Given that the centroid energy of the giant monopole resonance (GMR) scales as the square-root of the incompressibility coefficient [78], the impact of the density dependence of the symmetry energy on the distribution of monopole strength may be significant. In particular, a systematic study of GMR energies as a function of neutron-proton asymmetry—especially along isotopic chains [64, 65, 66]—may be of enormous value. For example ^{90}Zr , a nucleus with a well-developed GMR peak but with a neutron-proton asymmetry of only $\alpha_{90}^2 = (0.111)^2 = 0.012$, is ideal for determining the incompressibility coefficient of symmetric nuclear matter K_0 . Once K_0 has been determined, one may then use the GMR in ^{208}Pb , with a value of $\alpha_{208}^2 = (0.212)^2 = 0.045$ four times as large, to constrain K_τ [79]. It is important to underscore that one measurement alone is not sufficient. For example, NL3 is known to predict a rapid increase with density for both symmetric nuclear matter and the symmetry energy. In particular, it was possible for NL3 to be consistent with the GMR in ^{208}Pb by having a large value of K_τ compensate for a correspondingly large value of K_0 [80]. However, this was no longer possible in the case of ^{90}Zr because its significant lower value of α^2 . Thus, NL3 was found to overestimate the GMR in ^{90}Zr by about 0.7 MeV, which is significantly larger than the 0.2 MeV experimental error [79].

We conclude this section with a brief summary of the relevant moments of the distribution of strength that will be displayed in Sec. 3. In the long wavelength limit the distribution of isoscalar monopole strength $R(\omega; E0)$ is directly related to the longitudinal response defined in Eq. (6) by the following expression:

$$R(\omega; E0) = \lim_{q \rightarrow 0} \left(\frac{36}{q^4} \right) S_L(q, \omega; E0). \quad (23)$$

In turn, moments of the distribution of isoscalar monopole strength are defined as suitable energy weighted sums. That is,

$$m_n(E0) \equiv \int_0^\infty \omega^n R(\omega; E0) d\omega. \quad (24)$$

Widely used in the literature are the energy weighted m_1 , energy unweighted m_0 , and inverse energy weighted m_{-1} sums. In particular, we will present results in Sec. 3 for the GMR centroid energies defined as $E_{\text{GMR}} = m_1/m_0$.

2.3 Isovector Giant Dipole Resonance

In a simple macroscopic picture the isovector giant dipole resonance (GDR) is perceived as an out of phase collective oscillation of neutrons against protons. Thus, the symmetry energy at sub-saturation densities acts as the restoring force. As in the case of the GMR, the distribution of isovector dipole strength $R(\omega; E1)$ may be extracted from the longitudinal response defined in Eq. (6). That is, in the long wavelength approximation we obtain

$$R(\omega; E1) = \lim_{q \rightarrow 0} \left(\frac{9}{4\pi q^2} \right) S_L(q, \omega; E1). \quad (25)$$

We note that the relevant transition operator extracted from Eq. (7) for the isovector dipole mode is given by

$$\hat{\rho}_3(\mathbf{q}) \propto \int d^3r \bar{\psi}(\mathbf{r}) j_1(qr) Y_{1\mu}(\hat{\mathbf{r}}) \gamma^0 \tau_3 \psi(\mathbf{r}), \quad (26)$$

where j_1 is a spherical Bessel function and $Y_{1\mu}$ is a spherical harmonic. We have mentioned that in finite nuclei, especially those with a significant neutron excess, there may be significant mixing between isoscalar and isovector modes. In the particular case of dipole resonances, the isovector GDR will mix with the isoscalar mode, so care must be taken in handling properly the spurious center of mass motion. However, we stress that in the context of a self-consistent RPA framework, no modification to the transition operator given in Eq. (26) is required, as the formalism by itself and nothing else should push all spurious strength to zero excitation energy [75].

Moments of the distribution of isovector dipole strength may be defined in analogy to Eq. (24) as follows:

$$m_n(E1) \equiv \int_0^\infty \omega^n R(\omega; E1) d\omega. \quad (27)$$

Of great relevance are the energy weighted m_1 and inverse energy weighted m_{-1} sums. In particular, m_1 satisfies a classical energy weighted sum rule (EWSR):

$$m_1(E1) = \frac{9\hbar^2}{8\pi M} \left(\frac{NZ}{A} \right) \approx 14.8 \left(\frac{NZ}{A} \right) \text{fm}^2 \text{MeV}. \quad (28)$$

Note that the EWSR is related to the total photoabsorption cross section $\sigma(\omega)$ and the corresponding TRK sum rule. That is,

$$\int_0^\infty \sigma(\omega) d\omega = \frac{16\pi^3 e^2}{9 \hbar c} m_1 \approx 60 \left(\frac{NZ}{A} \right) \text{MeV mb}. \quad (29)$$

The power of the sum rules is that in principle they are independent of the details of the interaction. In practice, however, the classical sum rules are only valid in the absence of exchange and momentum dependent forces [7]. The appearance of such forces modifies the classical sum rules and their impact is traditionally accounted for by multiplying the right-hand side of Eqs. (28-29) by a factor of $(1 + \kappa_{\text{TRK}})$ with $\kappa_{\text{TRK}} \approx 0.2$ [7]. Also note that the classical sum rules were derived using a non-relativistic formalism so one may also need to correct for relativistic effects; we will assume here that such relativistic effects have been also incorporated into κ_{TRK} .

Besides the EWSR, the inverse energy weighted sum m_{-1} is of critical importance because its sensitivity to the density dependence of the symmetry energy [81, 82, 83, 84]. Note that the electric dipole polarizability α_{D} is simply related to m_{-1} :

$$\alpha_{\text{D}} = \frac{8\pi}{9} e^2 m_{-1}. \quad (30)$$

Recently, a high-resolution measurement of the electric dipole polarizability in ^{208}Pb was performed at the Research Center for Nuclear Physics (RCNP) using polarized

proton inelastic scattering at forward angles [85,86]. The great virtue of this experiment is that at forward angles Coulomb excitation dominates, thereby making the extraction of α_D free from strong-interaction uncertainties. The reported value of α_D in ^{208}Pb is [85,86]

$$\alpha_D^{208} = (20.1 \pm 0.6) \text{ fm}^3. \quad (31)$$

For additional details on this landmark experiment and on how it may be used to constrain the density dependence of the symmetry energy, see the contribution to this volume by Tamii, von Neumann-Cosel, and Poltoratska.

Although microscopic MF+RPA calculations of α_D will be presented in the next section, we close this section by providing insights from the macroscopic liquid droplet model to elucidate the connection between the dipole polarizability and the density dependence of the symmetry energy [84,87]. In particular, following closely the recent analysis by Roca-Maza and collaborators, one finds a simple relation between α_D and two fundamental parameters of the symmetry energy, namely, J and L . That is [84],

$$\alpha_D^{\text{DM}} \approx \frac{\pi e^2}{54} \frac{A \langle r^2 \rangle}{J} \left[1 + \frac{5L}{3J} \epsilon_A \right]. \quad (32)$$

where $\langle r^2 \rangle$ is the mean-square radius of the nucleus and $\epsilon_A = (\rho_0 - \rho_A)/3\rho_0$ accounts for the difference between the saturation density ρ_0 and an appropriate average nuclear density ρ_A . Note that this expression suggests that J and L may be separately constrained from measuring α_D in a few nuclei. Moreover, it indicates that the dipole polarizability times the symmetry energy at saturation density ($\alpha_D J$) should be better correlated to L than α_D alone [84].

3 Results

Having developed the formalism required to compute the distribution of both monopole and dipole strength, we are now in a position to discuss the predictions of our relativistic RPA calculations. However, before doing so it is convenient to introduce the models used in this work and their associated predictions for the bulk parameters of infinite nuclear matter. We start by displaying in Table 1 the model parameters for the various relativistic density functionals used in this review. Note that the parameters are defined according to the Lagrangian density given in Eq. (5). Included in this set are the two accurately-calibrated density functionals: NL3 [88,89] and FSUGold (or “FSU” for short) [90]. Relative to NL3—a model enormously successful in reproducing masses and charge radii over the whole nuclear chart—FSUGold includes two additional parameters (ζ and A_v) that are used to soften both the EOS of symmetric nuclear matter and the symmetry energy. The IU-FSU effective interaction was conceived in response to the recent interpretation of X-ray observations by Steiner, Lattimer, and Brown that suggests that FSUGold predicts neutron star radii that are too large and a maximum stellar mass that is too small [91]. As seen in Table 1, stiffening the EOS of symmetric nuclear

matter by reducing ζ and softening the symmetry energy by increasing A_v provides a simple and efficient procedure to overcome these problems [92]. Finally, the last three effective interactions labeled as TAMUC-FSU (or “TF” for short) were created in response to the provocative result reported by the PREX collaboration, namely, that the neutron-skin thickness of ^{208}Pb is significantly larger than predicted by a large set of theoretical calculations. Indeed, the PREX central value of $r_{\text{skin}}^{208} \approx 0.33$ fm is particularly intriguing. Hence, the TF interactions (calibrated to $r_{\text{skin}}^{208} = 0.25, 0.30,$ and 0.33 fm, respectively) were created to test whether such a thick neutron-skin in ^{208}Pb is already incompatible with laboratory experiments or astrophysical observations [93].

Note that although the parameters of the IU-FSU and TAMUC-FSU models do not follow from a strict optimization procedure, a significant effort was made in reproducing some bulk parameters of infinite nuclear matter as well as some critical properties of finite nuclei. Indeed, predictions from various bulk parameters of infinite nuclear matter as defined in Eqs. (17) and (22) are listed in Table 2. In particular, the variation among those bulk parameters that are sensitive to nuclear masses is relatively small: $\Delta\rho_0 \approx 5\%$, $\Delta\epsilon_0 \approx 2\%$, and $\Delta J \approx 40\%$. Note that even though ΔJ does not appear to be small, Eq. (21) suggests that the relevant combination that enters the determination of nuclear masses is $\alpha^2 \Delta J$; for stable nuclei $\alpha^2 \Delta J \lesssim 6\%$. Although accurately measured ground-state properties are fairly insensitive to the incompressibility coefficient of symmetric nuclear matter, the calibration of modern relativistic functionals now aims to incorporate GMR energies from a few critical nuclei, such as ^{90}Zr and ^{208}Pb [94]. This should help reduce the uncertainty in K_0 . Note, however, that at present even the sign of the skewness parameter Q_0 remains unconstrained. Also poorly constrained are the symmetry energy parameters L and K_{sym} , with the former displaying a variation of more than a factor of two and the latter with a sign that still remains undetermined. Not surprisingly, the symmetry energy contribution to the incompressibility coefficient K_τ —which involves a linear combination of L , K_{sym} , and Q_0 as shown in Eq. (22)—displays a variation of more than a factor of four. However, note that in spite of such a large variation, the sign of K_τ is predicted to be negative in all the models. This fact is driven by the large and negative coefficient (of -6) in front of L in the expression for K_τ . Given the very strong correlation between L and the neutron-skin thickness of ^{208}Pb , K_τ is likely to be negative for all realistic models that predict a neutron-rich skin in ^{208}Pb . Finally, the last two columns display the incompressibility coefficient of neutron-rich matter with a neutron-proton asymmetry equal to that of ^{90}Zr and ^{208}Pb , respectively. Ignoring the predictions from the NL3 parametrization, as it did not include information on GMR energies in its calibration, the variations amount to $\Delta K_{90} \approx 10\%$ and $\Delta K_{208} \approx 3\%$. As GMR centroid energies scale as $E_{\text{GMR}}(\alpha) \propto \sqrt{K_0(\alpha)}$, the anticipated errors in the respective energies should be half as large. Given that FSUGold is consistent with the GMR centroid energies in both ^{90}Zr

Model	$m_s(\text{MeV})$	g_s^2	g_v^2	g_ρ^2	$\kappa(\text{MeV})$	λ	ζ	A_v
NL3	508.194	104.3871	165.5854	79.6000	3.8599	-0.015910	0.00	0.00000
FSUGold	491.500	112.1996	204.5469	138.4701	1.4203	+0.023760	0.06	0.03000
IU-FSU	491.500	99.4266	169.8349	184.6877	3.3808	+0.000296	0.03	0.04600
TAMUC-FSUa	502.200	106.5045	176.1780	97.3556	3.1824	-0.003470	0.02	0.01267
TAMUC-FSUb	497.100	104.3524	176.2026	90.5000	3.1163	-0.003021	0.02	0.00000
TAMUC-FSUC	496.800	113.9565	198.0546	103.4000	2.6079	-0.001864	0.02	0.00000

Table 1. Model parameters for all the relativistic density functionals used in the text. Masses for the isoscalar-vector meson, isovector-vector meson, and nucleon have been fixed at $m_v = 782.5$ MeV, $m_\rho = 763$ MeV, and $M = 939$ MeV, respectively.

and ^{208}Pb , we expect that all models—with the possible exception of NL3—should also be consistent with experiment. Note that whereas GMR constraints on the symmetry energy are hindered by the short lever arm multiplying K_τ (i.e., α^2), isovector dipole excitations probe directly the symmetry energy. In particular, insights from the droplet model suggest that measurements of the electric dipole polarizability for a variety of nuclei should simultaneously constrain the value and slope (J and L) of the symmetry energy at saturation density. Ultimately, the determination of the density dependence of the symmetry energy will require a concerted effort involving both laboratory experiments and astrophysical observations. This special volume goes a long way towards fulfilling this goal.

3.1 Isoscalar Giant Monopole Resonance

We start this section by displaying in Fig. 3 relativistic RPA predictions for the distribution of isoscalar monopole strength for nuclei ranging from ^{90}Zr to ^{208}Pb . As it was underscored in the previous section, a systematic study on nuclei with a wide range of neutron-proton asymmetries and well developed GMR peaks is required to constrain both K_0 and K_τ . As it is evident from the figure, the heavier the nucleus the stronger the collective effects. Given the strong and attractive nature of the isoscalar residual interaction, a softer and better developed GMR peak is generated with increasing A . Note that the predicted escape width is generated exactly within the non-spectral approach. However, the predicted width is in general smaller than experiment as more complicated excitations (such as those involving many particles and holes) are beyond the scope of the RPA approach. Although theoretical RPA calculations are unable to account for the full experimental width, they should be able to provide a fairly good description of the centroid energy $E_{\text{GMR}} = m_1/m_0$. To this end, predictions for the centroid energy of the six nuclei considered in Fig. 3 are listed in Table 3 together with the corresponding experimental values [60, 61, 62, 63, 64, 65, 66]. The numbers in parenthesis correspond to the range of excitation energies used to compute the moments of the distribution of strength [see Eq. (24)]. The same information is displayed in graphical form in Fig. 4 for ^{90}Zr , ^{116}Sn , ^{144}Sm , and ^{208}Pb . It is evident from the figure that regardless of the value of K_0 and the stiffness of the symmetry energy, all models—with the possible exception of NL3—cluster around each other. Indeed, with

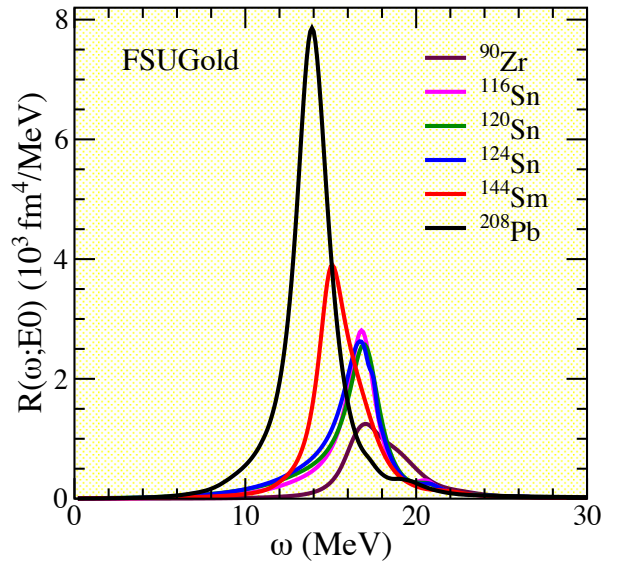


Fig. 3. (color online) Distribution of isoscalar monopole strength for nuclei ranging from ^{90}Zr to ^{208}Pb as predicted by relativistic RPA calculations using the FSUGold effective interaction [90].

the exception of NL3, the variation in the predictions of these models is limited to at most 2%. This suggests that centroid energies of monopole resonances—even those of nuclei with a large neutron excess—are unable to place stringent constraints on the density dependence of the symmetry energy [93].

3.1.1 Why is Tin so soft?

We just showed how predictions from a variety of models with widely different bulk properties can reproduce the GMR centroid energies of ^{90}Zr , ^{144}Sm , and ^{208}Pb . However, on closer examination these models appear to overestimate the GMR energy in all of the Tin isotopes. Indeed, whereas the theoretical spread among these model (not including NL3) amounts to at most 1%, their predictions are incompatible with experiment. Thus, the question of “why is Tin so soft?” has been raised to the forefront of nuclear structure [11, 64, 65, 95, 96, 97, 98, 99]. To underscore the challenge facing nuclear structure we display in Fig. 5 the distribution of isoscalar monopole strength in all

Model	ρ_0 (fm $^{-3}$)	ε_0	K_0	Q_0	J	L	K_{sym}	K_τ	K_{90}	K_{208}
NL3	0.148	-16.24	271.54	209.46	37.29	118.19	100.88	-699.41	262.90	240.24
FSUGold	0.148	-16.30	230.00	-522.74	32.59	60.52	-51.31	-276.87	226.59	217.62
IU-FSU	0.155	-16.40	231.33	-291.12	31.30	47.21	28.53	-195.29	228.92	222.59
TAMUC-FSUa	0.149	-16.23	245.00	-150.77	35.05	82.50	-68.37	-512.60	238.67	222.06
TAMUC-FSUB	0.149	-16.40	250.00	-156.60	40.07	122.53	45.88	-612.54	242.44	222.59
TAMUC-FSUC	0.148	-16.47	260.49	92.86	43.67	135.25	51.64	-808.04	250.51	224.33

Table 2. Bulk parameters of infinite nuclear matter at saturation density ρ_0 . The quantities ε_0 , K_0 , and Q_0 represent the binding energy per nucleon, incompressibility coefficient, and skewness parameter of symmetric nuclear matter. Similarly, J , L , and K_{sym} represent the energy, slope, and curvature of the symmetry energy; see Eq. (17). K_τ is the symmetry energy contribution to the incompressibility coefficient defined in Eq. (22). Finally, K_{90} and K_{208} correspond to the incompressibility coefficient of asymmetric nuclear matter with a neutron-proton asymmetry equal to that of ^{90}Zr ($\alpha_{90} = 0.111$) and ^{208}Pb ($\alpha_{208} = 0.211$), respectively. All quantities are in MeV unless otherwise indicated.

Model	$^{90}\text{Zr}(10-26)$	$^{116}\text{Sn}(10-23)$	$^{120}\text{Sn}(10-20)$	$^{124}\text{Sn}(10-20)$	$^{144}\text{Sm}(8-23)$	$^{208}\text{Pb}(8-23)$
NL3	18.62	17.09	16.76	16.52	16.14	14.33
FSUGold	17.98	16.55	16.24	16.08	15.63	14.02
IU-FSU	17.87	16.51	16.29	16.14	15.61	14.17
TAMUC-FSUa	18.06	16.59	16.32	16.10	15.65	13.96
TAMUC-FSUB	18.09	16.61	16.31	16.08	15.67	13.89
TAMUC-FSUC	18.17	16.66	16.36	16.11	15.72	13.89
Experiment						
TAMU	17.89 \pm 0.20	16.07 \pm 0.12		14.50 \pm 0.14	15.39 \pm 0.28	14.17 \pm 0.28
RCNP	18.10 \pm 0.10	16.19 \pm 0.10	15.55 \pm 0.10	15.27 \pm 0.10	16.00 \pm 0.35	13.90 \pm 0.20

Table 3. GMR Centroid energies predicted by the relativistic models discussed in the text. Quantities in parenthesis represent the minimum (ω_{min}) and maximum (ω_{max}) values used in Eq. (24) to compute various moments of the distribution of strength. Experimental values were obtained at TAMU [60,61] and RCNP [62,63,64,65,66].

stable, neutron-even Tin isotopes measured at RCNP [64, 65]. Also shown in the figure are relativistic RPA predictions obtained with the “stiff” NL3 and “soft” FSUGold interactions. Note that for clarity the theoretical peak energy has been normalized to the experimental data. The RCNP experiment aimed to probe the incompressibility of neutron-rich matter by measuring the GMR along a chain of isotopes with a neutron excess in the range $\alpha = 0.11-0.19$. Clearly discernible in the figure is the larger width of the experimental distribution relative to the theoretical predictions. This is expected, as RPA calculations are unable to account for the complicated spreading width. What is not expected is the systematic hardening of the theoretical predictions—especially given that FSUGold reproduces the centroid energies of ^{90}Zr , ^{144}Sm , and ^{208}Pb . To further elucidate this problem we display in Fig. 6 centroid energies obtained by integrating the distribution of monopole strength over the $\omega = 10-20$ MeV interval. Two points are worth emphasizing: (a) the value of the centroid energy in ^{112}Sn and (b) the softening of the mode as a function of A . Given that the neutron excess in ^{112}Sn is small ($\alpha^2 \approx 0.01$), the value of its centroid energy is mostly sensitive to K_0 with only a 1% correction from K_τ . This is clearly reflected in the predictions of NL3 (with $K_0 = 271.5$ MeV) and FSUGold (with $K_0 = 230.0$ MeV). In particular, the FSUGold prediction is within 1% of the (upper limit of the) experimental value. However, the experiment suggests a very rapid softening

of the mode with mass number that is not reproduced by either NL3 or FSUGold. Note that the falloff with A is controlled—at least in infinite nuclear matter—by K_τ so the softening predicted by NL3 is indeed faster than that of FSUGold, but clearly nowhere as fast as required by the experiment. Hence, the 1% discrepancy ^{112}Sn between FSUGold and experiment, increases by a factor of 4—or to 0.7 MeV which is significantly larger than the 0.1 MeV experimental error. Also shown in Fig. 6 are the predictions from a “Hybrid” model that was created with the sole purpose of reproducing the RCNP data [11]. In particular, the Hybrid model has the same soft incompressibility coefficient as FSUGold ($K_0 = 230$ MeV) but a considerable stiffer symmetry energy ($K_\tau = -565$ MeV). Note that these bulk parameters agree with the recommended values of $K_0 = 240 \pm 10$ MeV and $K_\tau = -550 \pm 100$ MeV given in Ref. [64]. Unquestionably, the Hybrid model produces a significant improvement in the description of the data. Indeed, accounting for the experimental errors, the theoretical predictions fall within 0.1 MeV of the experimental data along the full isotopic chain. However, the falloff with A is still not as rapid as required by experiment. Yet, the Hybrid model suffers from an ever more serious problem: it underestimates the GMR centroid energy in ^{208}Pb by almost 1 MeV; see also Ref. [97]. Given that the solution to the problem of the softness of Tin should not come at the expense of sacrificing the overall quality of the model, we must conclude that the Hybrid model is unrealistic.

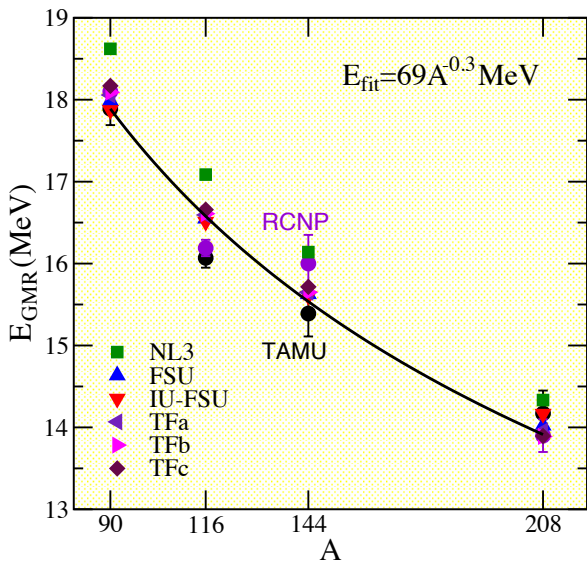


Fig. 4. (color online) GMR centroid energies ($E_{\text{GMR}} = m_1/m_0$) in ^{90}Zr , ^{116}Sn , ^{144}Sm , and ^{208}Pb , as predicted by the relativistic effective interactions used in the text. Also shown in the figure are experimental measurements reported by TAMU [60, 61] and RCNP [62, 63, 64, 65, 66]. The black line represents a best fit to the FSU predictions of the form $E_{\text{fit}} = 69 A^{-0.3}$.

So after more than 5 years since the publication of the experimental data, the answer to the question of “why is Tin so soft?” continues to elude us. Note that the softness of Tin has been recently confirmed in the nearby isotopic chain in Cadmium [100]. It has been proposed that the failure to reproduce the GMR energies in Sn, and now in Cd, may be due to missing physics unrelated to the bulk incompressibility of neutron-rich matter. One suggestion that has received considerable attention involves the superfluid character of the Tin isotopes [101, 102, 103, 104, 105]. Although the conclusions have been mixed and seem to depend strongly on the character of the pairing force, it is safe to assume that pairing correlations do not provide a robust softening mechanism. Regrettably then, we are forced to conclude that the softness of both Tin and Cadmium remains an important open problem.

3.2 Isovector Giant Dipole Resonance

Whereas probing to the symmetry energy via the GMR is hindered by the relative small neutron-proton asymmetry of stable nuclei, the isovector dipole mode provides a direct access to its density dependence. Indeed, the GDR is commonly perceived as an out of phase oscillation of neutrons against proton with the symmetry energy acting as the restoring force. In particular, models with a stiff symmetry energy (*i.e.*, models with an energy that increases rapidly with increasing density) predict small values for the symmetry energy at the sub-saturation densities of relevance to the excitation of this mode. As a result, models with a stiff symmetry energy, and thus large values of

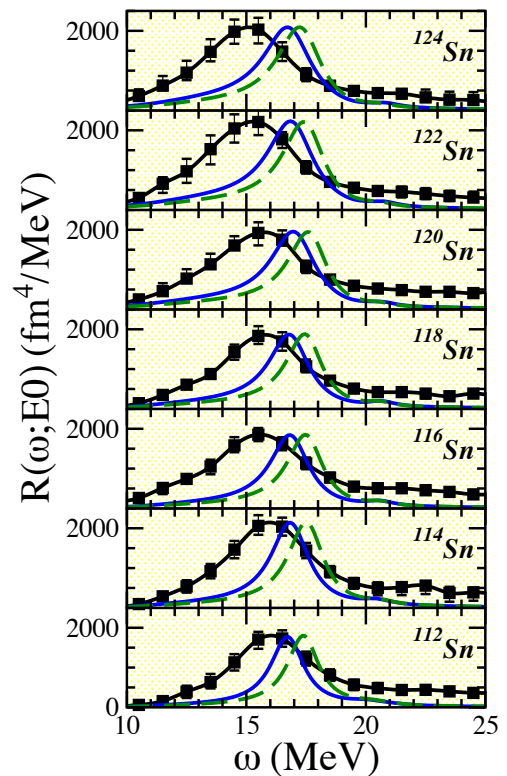


Fig. 5. (color online) Comparison between the distribution of isoscalar monopole strength in all stable, neutron-even Tin isotopes measured at RCNP [64, 65] against the theoretical predictions of NL3 (green dashed line) and FSUGold (blue solid line).

L , predict a distribution of dipole strength that is both enhanced and softened relative to their softer counterparts. However, although the distribution of dipole strength is sensitive to the density dependence of the symmetry energy, the energy weighted sum is not. This is because the m_1 moment of the distribution is “protected” by the classical model independent EWSR [see Eq. (28)]. A far better isovector indicator is the electric dipole polarizability which is directly proportional to the inverse EWSR [81, 82, 83, 84]. The dipole polarizability is particularly attractive because here the softening and enhancement are intensified as one weighs the response with ω^{-1} . This point is nicely illustrated in Fig. 7 which displays the inverse energy weighted distribution of isovector dipole strength in ^{208}Pb for the “family” of FSUGold interactions. The virtue of introducing such family of interactions is that one can assess systematic changes in a given observable as a single bulk parameter of the EOS is modified. In the particular case of the FSU family of interactions, one modifies the density dependence of the symmetry energy—essentially the value of L —while leaving the isoscalar sector intact [31]. Indeed, all models displayed in Fig. 7 share the same value of ρ_0 , ε_0 , K_0 , and Q_0 . Note that the models displayed in the figure are labeled according to their value of L . As mentioned earlier, the stiffer the symmetry energy the larger and softer the response. This trend be-

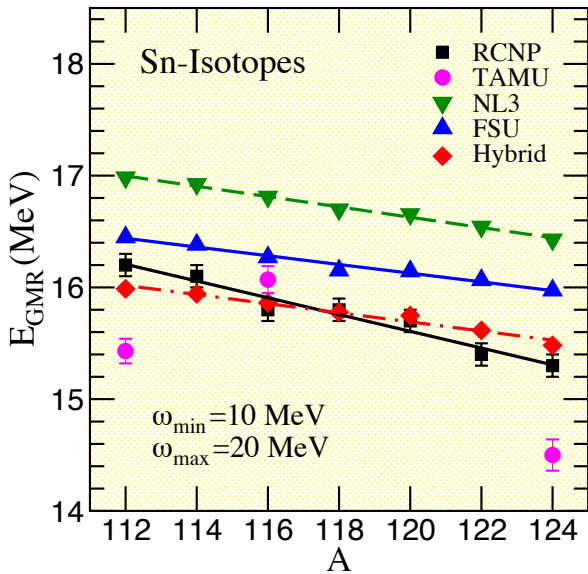


Fig. 6. (color online) Comparison between the GMR centroid energies in all stable, neutron-even Tin isotopes measured at RCNP [64,65] against the theoretical predictions of NL3 (green down-triangles), FSUGold (blue up-triangles), and the Hybrid model (red diamonds) introduced in Ref. [11]. Also shown (magenta circles) are measurements from the Texas A&M group [60,61] for $^{112,116,124}\text{Sn}$.

comes evident in the inset to the figure which displays the running sum $m_{-1}(\omega)$ defined as

$$m_{-1}(\omega) \equiv \int_0^\omega z^{-1} R(z; E1) dz. \quad (33)$$

Although there is already some separation at lower excitation energies, by the time that one has integrated over the region of the GDR the model dependence becomes apparent. Hence a powerful correlation emerges: the larger the value of L , the larger the dipole polarizability in ^{208}Pb . Moreover, this correlation may be framed in the form of a powerful “data-to-data” relation: the larger the neutron-skin thickness of ^{208}Pb the larger its dipole polarizability.

Such a data-to-data relation between the neutron-skin thickness and electric dipole polarizability in ^{208}Pb is displayed in Fig. 8 for a large set of 48 relativistic and non-relativistic energy density functionals [83]. Even though a clear linear trend between α_D^{208} and r_{skin}^{208} is observed, one also notices a significant scatter in the predictions of these models. However, note that each set of systematically varied models (all models with the exception of the standard Skyrme interactions depicted with the black triangles) display an almost perfect correlation. An overall correlation coefficient of 0.77 is found when the predictions from all 48 EDFs are included. Note that by imposing the recent experimental constraint from α_D^{208} [85,86] several models, especially those with a very stiff symmetry energy, may already be ruled out. Remarkably, if the updated PREX experiment (PREX-II)—with a projected uncertainty of 0.06 fm—finds that its central value of $r_{\text{skin}}^{208} = 0.33$ fm re-

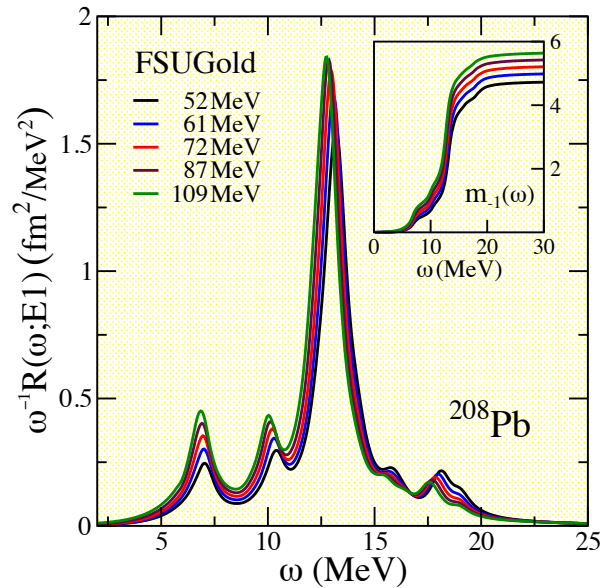


Fig. 7. (color online) Distribution of inverse energy weighted isovector dipole strength for ^{208}Pb as predicted by the FSUGold family of effective interactions. The labels indicate the slope of the symmetry energy L predicted by each model and the inset shows the running sum $m_{-1}(\omega)$ as defined in Eq. (33).

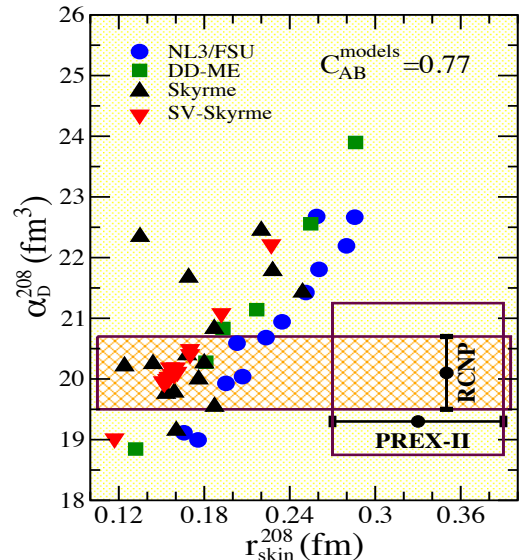


Fig. 8. (Color online) Predictions from 48 nuclear EDFs for the electric dipole polarizability and neutron-skin thickness of ^{208}Pb as discussed in Ref. [83]. Constrains from both RCNP [85,86] and PREX [19] (the latter assuming a projected 0.06 fm error) have been incorporated into the plot.

mains intact, then all 48 models displayed in the figure will be ruled out!

Although the correlation between α_D^{208} and r_{skin}^{208} displayed in Fig. 8 is evident, insights from the droplet model [Eq. (32)] suggest that a far better correlation involves the product of α_D^{208} times the symmetry energy at saturation

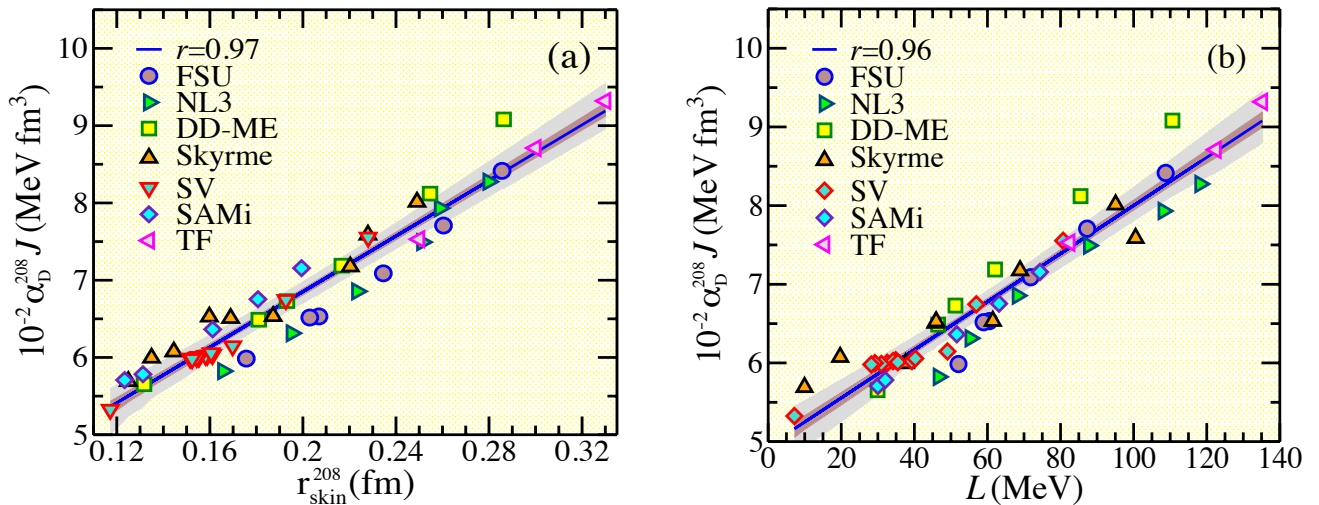


Fig. 9. (Color online) (a) Predictions from a large number of EDFs for the electric dipole polarizability of ^{208}Pb times the symmetry energy at saturation density as a function of the neutron-skin thickness of ^{208}Pb . (b) Same as in (a) but now as a function of the slope of the symmetry energy L . The two shaded regions represent the 99.9% and 70% confidence bands, respectively. These results were first reported in Ref. [84].

density J predicted by each model [84]. Thus, we display in Fig. 9 the product $\alpha_D^{208}J$ as a function of both r_{skin}^{208} (in the left-hand panel) and L (in the right-hand panel). Remarkably, the large spread in the model predictions seen in Fig. 8 has been practically eliminated. Indeed, the figure validates (with correlation coefficients of 0.97 and 0.96) that the product $\alpha_D^{208}J$ is far better correlated to both r_{skin}^{208} and L than the polarizability alone. Note that the set of density functionals used in Fig. 9 now includes two additional EDFs, namely, TAMUC-FSU [93] and SAMi [106], with the former having a stiff and the latter a soft symmetry energy. Between them, they span a large range in neutron-skin thickness: $r_{\text{skin}}^{208} \approx (0.12\text{-}0.33)$ fm or equivalently $L \approx (30\text{-}135)$ MeV. Still, the predictions from both of these models fall comfortably within the confidence bands. We expect that during the next few years high-precision measurements of the electric dipole polarizability on a variety of nuclei will provide stringent constraints on the density dependence of the symmetry energy.

3.2.1 Pygmy Dipole Resonance

We conclude this section by discussing the interesting and often controversial topic of low energy dipole strength, the so-called Pygmy Dipole Resonance (PDR). Proposals on the possible existence of a new type of dipole oscillation in which the neutron skin vibrates against the isospin symmetric core date back to the early 1990's [107, 108]. Since then, state-of-the-art RPA calculations have been developed to predict the distribution of low-energy dipole strength and associated transition densities for a variety of neutron-rich nuclei [109, 110, 111, 112, 113, 114, 115, 116]. Given that stable heavy nuclei are neutron rich, one expects the emergence of low energy dipole strength as the nucleus develops a neutron-rich skin. Thus, it was sug-

gested that the PDR may be used as a constraint on the neutron skin of heavy nuclei [114] as well as on the density dependence of the symmetry energy, and ultimately on the properties of neutron stars [117]. In particular, the fraction of the energy weighted sum rule exhausted by the PDR was shown to be sensitive to the neutron-skin thickness of heavy nuclei [39, 114, 117, 118, 119]. Pioneering experiments on unstable neutron-rich isotopes in Sn, Sb, and Ni seem to support this assertion [119, 120, 121, 122]. For a recent review on the Pygmy Dipole Resonance see Ref. [123].

To observe the emergence of pygmy strength as the nucleus develops a neutron-rich skin, we display in Fig. 10 the distribution of isovector dipole strength $R(\omega; E1)$ for all neutron-even Sn isotopes from ^{100}Sn to ^{130}Sn . The results shown in the figure are obtained from RPA calculations using the FSUGold effective interaction [90]. The large collective structure in the $\omega \gtrsim 15$ MeV corresponds to the giant dipole resonance. The collective character of the GDR is associated with the coherent out of phase oscillation of neutrons against protons and is observed in all isotopes regardless of neutron excess. Moreover, as is characteristic of such a giant resonance, it exhausts a large fraction of the EWSR. But clearly not all! The emergence of low-energy dipole strength with increasing neutron excess is clearly discernible in the figure. Indeed, the progressive addition of neutrons results in a well developed, albeit small, low-energy resonance. Note that the PDR is barely visible below ^{108}Sn , increases gradually beyond ^{110}Sn , and finally saturates at ^{120}Sn . This saturation effect is attributed to the filling of the $1h^{11/2}$ neutron orbital. Whereas the 12 neutrons filling the $1h^{11/2}$ orbital contribute to a systematic increase in the size of the neutron skin, high-angular momentum orbitals play a minor role in generating low-energy dipole strength [117].

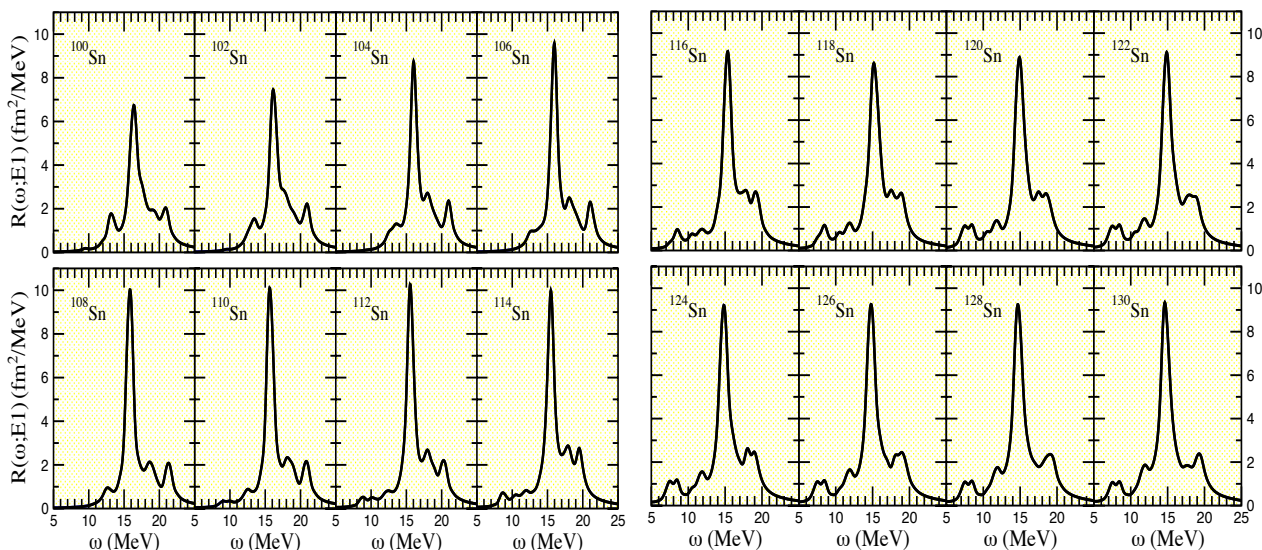


Fig. 10. (Color online) Distribution of isovector dipole strength for all neutron-even tin isotopes from ^{116}Sn to ^{130}Sn . Relativistic RPA calculations were carried out with the FSUGold effective interaction [90].

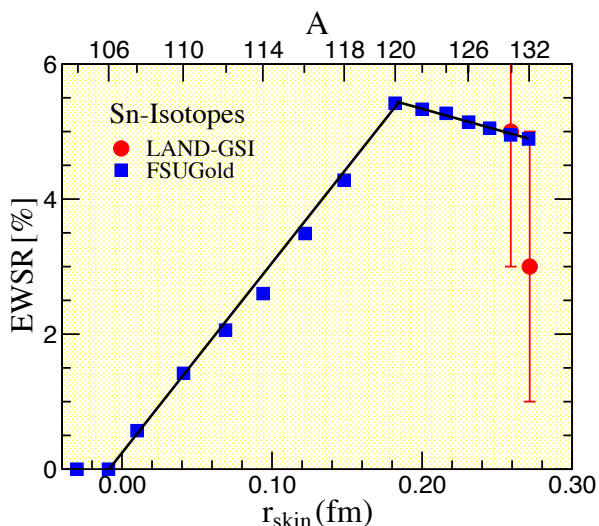


Fig. 11. (Color online) Fraction of the energy weighted sum rule contained in the PDR relative to that in the GDR for the isotopic chain in Sn. The experimental data is from Ref. [120].

The fraction of the EWSR contained in the PDR relative to that of the GDR is displayed in Fig. 11 as a function of neutron-skin thickness. Note that below ^{108}Sn , where there is no visible low-energy strength, the neutron-skin thickness of the various Sn-isotopes is negative. The experimental data is from the pioneering measurement on the unstable $^{130,132}\text{Sn}$ isotopes carried out by the LANDFRS collaboration at GSI [120]. The separation between low- and high-energy strength was chosen at $\omega = 10$ MeV. The linear correlation between r_{skin} and the fraction of dipole strength exhausted by the PDR justifies the assertion that the neutron excess is indeed responsible for the emergence of low-energy strength as the nucleus becomes

progressively more neutron rich. Moreover, the saturation of this effect due to the failure of the $1h^{11/2}$ neutron orbital to generate low-energy strength is also clearly visible. Unfortunately, at present the experimental error bars are too large to place significant constraints on the density dependence of the symmetry energy. However, by combining information on the the fraction of the EWSR exhausted by the PDR in both ^{132}Sn [120] and ^{68}Ni [121], Carbone and collaborators were able to constrain the slope of the symmetry energy to the range of $L = 64.8 \pm 15.7$ MeV [39].

In spite of this success, we believe that the reliance on the energy weighted sum rule suffers from two serious limitations. First, the classical EWSR is model independent so the sensitivity of the fraction exhausted by either the PDR or GDR to the symmetry energy must be modest. Second, in generating the EWSR one weighs the distribution of strength with the energy, thereby diminishing the impact of the PDR even further. In contrast, the inverse energy weighted sum rule does not suffer from any of these problems. First, as shown in Fig. 7, the inverse EWSR is sensitive to the density dependence of the symmetry energy. Second, the low-energy strength is now enhanced by weighting the distribution of strength with ω^{-1} . A nucleus with a significant amount of low-energy dipole strength is the exotic, neutron-rich ^{68}Ni isotope [121, 122]. The inverse energy weighted distribution of isovector dipole strength in ^{68}Ni is displayed on the left-hand panel of Fig. 12 for the family of FSUGold interactions. For reference, the fraction of the EWSR exhausted by the PDR in ^{68}Ni ranges from about 5% for the softest model to about 8% for the stiffest. In contrast, the fraction of the inverse EWSR contained in the PDR is significantly larger and varies in the range 20-25%; note that the corresponding fraction in ^{208}Pb —although still sizable—amounts to only 10% [see Fig. 7]. Moreover, the running sum $m_{-1}(\omega)$ depicted in the inset shows that there is significant model sensitivity to the

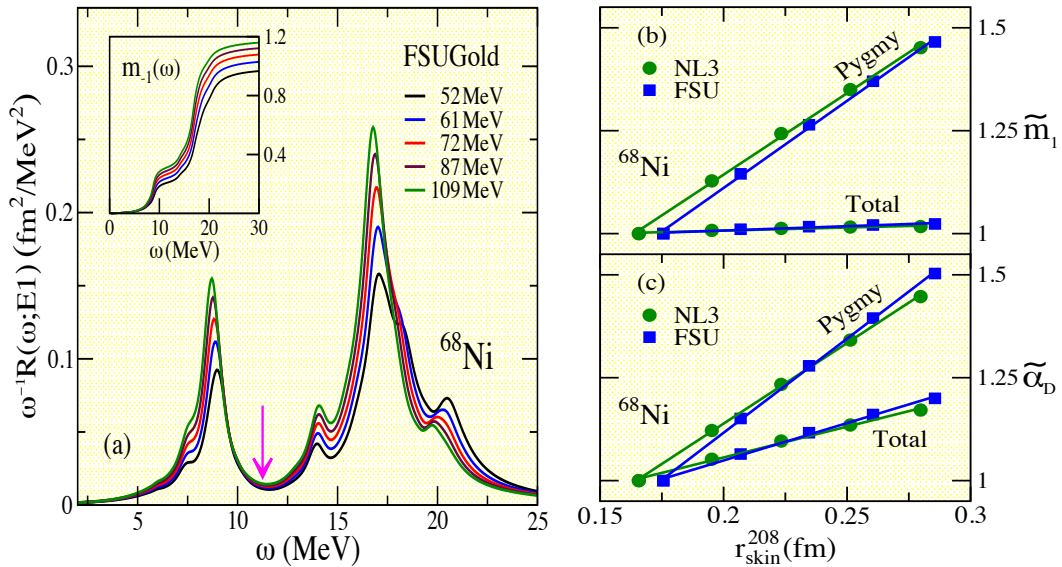


Fig. 12. (color online) (a) Distribution of inverse energy weighted isovector dipole strength in ^{68}Ni as predicted by the FSUGold family of effective interactions. The labels indicate the slope of the symmetry energy L predicted by each model and the inset shows the running sum $m_{-1}(\omega)$ as defined in Eq. (33). (b) Fractional change in the energy weighted sum rule of ^{68}Ni as a function of the neutron-skin thickness of ^{208}Pb as predicted by both NL3 and FSUGold. (c) same as (b) but now for the electric dipole polarizability.

amount of strength contained in both the PDR and the GDR. Although somehow arbitrary, the arrow located in the “dip region” is used to define the energy separating the low-energy from the high-energy region. To highlight these features we display in Figs. 12b and 12c NL3 and FSUGold predictions for the fractional changes in the total and Pygmy contributions to both m_1 and α_D as a function of the neutron-skin thickness of ^{208}Pb . Note that for ease of view we have plotted the fractional changes, *i.e.*, we have normalized the lowest point to one, and have used a “tilde” to denote these fractional changes. As anticipated, given that m_1 satisfies a classical sum rule, the sensitivity of the total EWSR to the density dependence of the symmetry energy is very weak; the slight deviation from one is due to the model dependence of the TRK enhancement factor. Conversely, the PDR displays a large sensitivity, albeit with a small signal, and could in principle be used to place constraints on the neutron-skin thickness of ^{208}Pb . Indeed, Carbone *et al.* have used measurements of the fraction of the EWSR exhausted by the PDR in both ^{132}Sn [120] and ^{68}Ni [121] to extract a value of $r_{\text{skin}}^{208} = 0.194 \pm 0.024$ fm [39]. However, the dipole polarizability enjoys several advantages over the EWSR. First, as far as the PDR is concerned, the sensitivity to r_{skin}^{208} is as large for α_D as it is for m_1 . Second, the total dipole polarizability is not protected by a classical sum rule. Thus, unlike the EWSR, the sensitivity of the total dipole polarizability to r_{skin}^{208} is significant. Finally—and most importantly—the total dipole polarizability is immune to the arbitrary separation of low-energy from high-energy strength. Indeed, whereas Fig. 12a shows a clear separation, experimentally the GDR tends to be quite broad, so deciding how much strength is contained in the PDR and how much in the tail of the

GDR is likely to be ill defined [123]. Thus, we conclude that the (total) electric dipole polarizability is a robust isovector indicator that provides critical insights into the density dependence of the symmetry energy. Nevertheless, the PDR is enormously interesting and one should devote time and resources to investigate its character and its connection, if any, to the neutron-skin thickness of heavy nuclei. Regardless, we believe that independent of the nature of the PDR, the emergence of low-energy dipole strength as nuclei develop a neutron-rich skin is an incontrovertible fact [82].

4 Conclusions and Outlook

In this review we have examined the critical role played by giant resonances in constraining the density dependence of the symmetry energy. In particular, we focused on the isoscalar monopole and isovector dipole resonances. We made this choice in response to the enormous experimental effort devoted to these resonances and for the critical physical insights that have emerged as a result.

Given that symmetric nuclear matter saturates, the incompressibility coefficient K_0 controls the energetics of the small oscillations around the saturation density. The GMR—or nuclear breathing mode—is our window into the incompressibility of nuclear matter. However, the accurate determination of K_0 requires the formation of a strong collective peak that exhausts most of the energy weighted sum rule. As such, one must rely on heavy nuclei, which are necessarily neutron-rich. This implies that experiments that measure the GMR in heavy nuclei (such as ^{208}Pb) probe the incompressibility coefficient of neutron-

rich matter, rather than that of symmetric matter. We showed in Eq. (22) that in terms of the neutron-proton asymmetry α , the incompressibility coefficient of asymmetric nuclear matter is given by $K(\alpha) = K_0 + K_\tau \alpha^2$. The sensitivity of GMR energies to the density dependence on K_τ . Indeed, K_τ is dominated by the slope of the symmetry energy L . Thus, it was believed that by measuring GMR centroid energies in ^{90}Zr and ^{208}Pb —nuclei with well-developed GMR peaks but values of α^2 that differ by a factor of four—one could simultaneously constrain K_0 and K_τ . Indeed, it was found that models with a relatively small K_0 and a soft the symmetry energy could reproduce experimental GMR energies in ^{90}Zr , ^{144}Sm , and ^{208}Pb . However, after a short period of relative calm, an experiment at the RCNP facility in Japan has muddled the waters. The goal of the experiment was to measure the distribution of monopole strength in all even- A , stable nuclei along the isotopic chain in Tin. The great advantage of such an experiment is that one could monitor the evolution of GMR strength as the isotope becomes progressively more neutron rich. However, the measurements revealed that self-consistent models that were successful in reproducing GMR energies in ^{90}Zr , ^{144}Sm , and ^{208}Pb overestimate the energy in all Sn-isotopes. Moreover, the discrepancy between theory and experiment appears to grow with neutron excess. Finally, we note that the softness of Tin has been extended to the neighboring isotopic chain in Cadmium. Hence, we must conclude—in spite of considerable effort—that the question of “*why is Tin so soft?*” remains unanswered.

In the case of the isovector dipole resonance, the symmetry energy acts as the restoring force. Given that the excitation of this mode results in the spatial separation of two dilute quantum fluids, one neutron rich and the other one proton rich, the GDR probes the symmetry energy at sub-saturation densities. This suggests that the distribution of dipole strength for models with a stiff symmetry energy is softened and enhanced relative to models having a soft symmetry energy. However, this sensitivity is eroded as one computes the energy weighted sum, which is protected by a classical sum rule. Instead, an observable that is particularly sensitive to the symmetry energy is the electric dipole polarizability (or inverse energy weighted sum) as here the softening and the enhancement act in tandem. Indeed, a powerful data-to-data relation may be established in this case: the thicker the neutron-skin thickness of ^{208}Pb the larger the dipole polarizability. We note, however, that although not strictly a data-to-data relation, a far stronger correlation emerges as one multiplies the dipole polarizability by the symmetry energy at saturation density [see Fig. 9]. Finally, we addressed the intriguing role of the pygmy dipole resonance in constraining the density dependence of the symmetry energy. Undeniably, we find a strong correlation between the emergence of low-energy dipole strength and the development of a neutron-rich skin along the isotopic chain in Tin. What is unclear at this juncture—but should be explored further—is whether one could cleanly separate

the low energy pygmy strength from the tail of the giant dipole resonance. Regardless of whether this is possible, the total electric dipole polarizability was found to be a strong isovector indicator.

In summary, the distribution of isoscalar monopole strength has been found to be sensitive to the density dependence of the symmetry energy. Unfortunately, this sensitivity is hindered by the relatively small neutron excess of the stable nuclei explored to date. In addition, we continue to puzzle after more than 5 years over the question of “*why is Tin so soft?*” Based on these facts, we strongly encourage measurement of the distribution of monopole strength in exotic nuclei at next generation facilities. In particular, mapping centroid energies outside the stable ^{112}Sn to ^{124}Sn region is sure to prove invaluable. Moreover, the electric dipole polarizability α_D has been found to be sensitive to the density dependence of the symmetry energy. Moreover, the combination of $\alpha_D^{208} J$ was seen to be very strongly correlated (with a correlation coefficient of 0.97) to the neutron-skin thickness of r_{skin}^{208} . Although photo-absorption experiments have been used for decades to probe the structure of the GDR, it is critical to delve into the low-energy region for a proper evaluation of α_D ; in ^{68}Ni the PDR alone accounts for 25% of the dipole polarizability. Here too the systematic exploration of the isovector dipole strength along the chain of Sn-isotopes, for both stable and exotic nuclei, may prove priceless. In regards to theory, the need to provide meaningful uncertainties in theoretical predictions of physical observables is a theme that is gaining significant momentum among the scientific community. Indeed, the search for an accurately calibrated microscopic theory that both predicts and provides well-quantified theoretical uncertainties is one of the founding pillars of modern nuclear energy density functionals [124, 125]. See the contribution to this volume by Nazarewicz, Reinhard, Satula, and Vretenar. The need to quantify model uncertainties in an area such as theoretical nuclear physics is particularly urgent as models that are fitted to experimental data are then used to extrapolate to the extremes of temperature, density, isospin asymmetry, and angular momentum. Inspired by some critical insights and ideas developed in the context of non-relativistic Skyrme functionals [81], a systematic statistical approach has been recently extended to the relativistic domain [126, 127]. An ambitious program aimed at calibrating future EDFs using ground-state properties of finite nuclei, their collective response, and neutron-star properties—supplemented by a proper covariance analysis—is well on its way [94]. A promising first step in this direction has been taken recently [128].

We conclude our contribution with some thoughts on the role of other physical observables addressed in this volume in constraining the density dependence of the symmetry energy. Unquestionably, such a challenging task will require a coherent effort involving the theoretical, experimental, and observational communities. From a theoretical perspective, powerful theoretical constraints that have emerged from the nearly universal behavior of pure neutron matter at very low densities have provided a strin-

gent limit on the slope of the symmetry energy [40,41,42]. See the contributions to this volume by Gandolfi *et al.* and Hebeler *et al.* Experimentally, we have already discussed at length the merits of giant resonances, especially the dipole polarizability, in constraining the symmetry energy. Together with the electric dipole polarizability, the neutron-skin thickness of heavy nuclei provide a powerful set of experimental constraints on the symmetry energy. The critical role of electroweak measurements of neutron densities is discussed in this volume by Horowitz, Kumar, and Michaels. Suffice it to say that elastic electron scattering is particularly advantageous as it provides a clean probe of neutron densities that is free from strong-interaction uncertainties. Finally, many contributions to this volume have addressed the imprint of the symmetry energy on astrophysical observables. Particularly promising is the accurate determinations of neutron-star radii—an observable sensitive to the density dependence of the symmetry energy at intermediate and high densities. Undoubtedly, enormous advances in land- and space-based observatories have brought us closer to one of the holy grails of neutron-star physics: mapping the mass-radius relation (see the contribution by Lattimer and Steiner to this volume). Ultimately, it will “take a village” to develop the effective strategies required to explore theoretically, experimentally, and observationally the remaining open questions in this exciting field.

Acknowledgments

I would like to thank my collaborators—too many to name here—for their support and critical insights. This work was supported in part by a grant from the U.S. Department of Energy DE-FD05-92ER40750.

References

1. P. Möller, J.R. Nix, W.D. Myers, and W.J. Swiatecki, *Atom. Data Nucl. Data Tabl.* **59**, 185 (1995).
2. P. Möller, J.R. Nix, and K.L. Kratz, *Atom. Data Nucl. Data Tabl.* **66**, 131 (1996).
3. P. Möller, W.D. Myers, H. Sagawa, and S. Yoshida, *Phys. Rev. Lett.* **108**, 052501 (2012).
4. J. Duflo, *Nucl. Phys.* **A576**, 29 (1994).
5. A. Zuker, *Nucl. Phys.* **A576**, 65 (1994).
6. J. Duflo and A. Zuker, *Phys. Rev. C* **52**, R23 (1995).
7. M.N. Harakeh and A. van der Woude, *Giant Resonances-Fundamental High-frequency Modes of Nuclear Excitation* (Clarendon, Oxford, 2001).
8. N. Paar, D. Vretenar E. Khan, and G. Colò, *Rept. Prog. Phys.* **70**, 691 (2007).
9. H. Sagawa, S. Yoshida, X.R. Zhou, K. Yako, and H. Sakai, *Phys. Rev.* **C76**, 024301 (2007).
10. X. Roca-Maza *et al.*, *Phys. Rev.* **C87** 034301 (2013).
11. J. Piekarewicz and M. Centelles, *Phys. Rev.* **C79**, 054311 (2009).
12. B.A. Brown, *Phys. Rev. Lett.* **85**, 5296 (2000).
13. R.J. Furnstahl, *Nucl. Phys.* **A706**, 85 (2002).
14. M. Centelles, X. Roca-Maza, X. Viñas, and M. Warda, *Phys. Rev. Lett.* **102**, 122502 (2009).
15. X. Roca-Maza, M. Centelles, X. Viñas, and M. Warda, *Phys. Rev. Lett.* **106**, 252501 (2011).
16. R. Hofstadter, *Rev. Mod. Phys.* **28**, 214 (1956).
17. T. Donnelly, J. Dubach, and I. Sick, *Nucl. Phys.* **A503**, 589 (1989).
18. I. Angeli and K. Marinova, *At. Data Nucl. Data Tables* **99**, 69 (2013).
19. S. Abrahamyan *et al.*, *Phys. Rev. Lett.* **108**, 112502 (2012).
20. C.J. Horowitz *et al.*, *Phys. Rev.* **C85**, 032501 (2012).
21. S.J. Pollock, E.N. Fortson, and L. Wilets, *Phys. Rev.* **C46**, 2587 (1992).
22. T. Sil, M. Centelles, X. Viñas, and J. Piekarewicz, *Phys. Rev.* **C71**, 045502 (2005).
23. J. Guena, M. Lintz, and M.A. Bouchiat, *Mod. Phys. Lett.* **A20**, 375 (2005).
24. J. Behr and G. Gwinner, *J. Phys.* **G36**, 033101 (2009).
25. M.B. Tsang, *et al.*, *Phys. Rev. Lett.* **92**, 062701 (2004).
26. L.W. Chen, C.M. Ko, and B.A. Li, *Phys. Rev. Lett.* **94**, 032701 (2005).
27. A.W. Steiner and B.A. Li, *Phys. Rev.* **C72**, 041601 (2005).
28. D.V. Shetty, S.J. Yennello, and G.A. Souliotis, *Phys. Rev.* **C76**, 024606 (2007).
29. M.B. Tsang *et al.*, *Phys. Rev. Lett.* **102**, 122701 (2009).
30. C.J. Horowitz and J. Piekarewicz, *Phys. Rev. Lett.* **86**, 5647 (2001).
31. C.J. Horowitz and J. Piekarewicz, *Phys. Rev.* **C64**, 062802 (2001).
32. C.J. Horowitz and J. Piekarewicz, *Phys. Rev.* **C66**, 055803 (2002).
33. J. Carriere, C.J. Horowitz, and J. Piekarewicz, *Astrophys. J.* **593**, 463 (2003).
34. A.W. Steiner, M. Prakash, J.M. Lattimer, and P.J. Ellis, *Phys. Rept.* **411**, 325 (2005).
35. B.A. Li and A.W. Steiner, *Phys. Lett.* **B642**, 436 (2006).
36. J.M. Lattimer and M. Prakash, *Phys. Rept.* **442**, 109 (2007).
37. F.J. Fattoyev and J. Piekarewicz, *Phys. Rev.* **C82**, 025810 (2010).
38. J. Piekarewicz, *Phys. Rev.* **C76**, 064310 (2007).
39. A. Carbone *et al.*, *Phys. Rev.* **C81**, 041301 (2010).
40. K. Hebeler, J. Lattimer, C. Pethick, and A. Schwenk, *Phys. Rev. Lett.* **105**, 161102 (2010).
41. A. Steiner and S. Gandolfi, *Phys. Rev. Lett.* **108**, 081102 (2012).
42. K. Hebeler, J. Lattimer, C. Pethick, and A. Schwenk, *Astrophys. J.* **773**, 11 (2013).
43. M. Tsang *et al.*, *Phys. Rev.* **C86**, 015803 (2012).
44. J.M. Lattimer, *Ann. Rev. Nucl. Part. Sci.* **62**, 485 (2012).
45. J.D. Walecka, *Annals Phys.* **83**, 491 (1974).
46. B.D. Serot, *Phys. Lett.* **B86**, 146 (1979).
47. R.J. Furnstahl and B.D. Serot, *Comments Nucl. Part. Phys.* **2**, A23 (2000).
48. P. Hohenberg and W. Kohn, *Phys. Rev.* **136**, B864 (1964).
49. W. Kohn and L.J. Sham, *Phys. Rev.* **140**, A1133 (1965).
50. W. Kohn, *Rev. Mod. Phys.* **71**(5), 1253 (1999).
51. R.J. Furnstahl, B.D. Serot, and H.B. Tang, *Nucl. Phys.* **A615**, 441 (1997).
52. R.J. Furnstahl, B.D. Serot, and H.B. Tang, *Nucl. Phys.* **A618**, 446 (1997).

53. J.J. Rusnak and R.J. Furnstahl, Nucl. Phys. **A627**, 495 (1997).
54. R.J. Furnstahl and J.C. Hackworth, Phys. Rev. **C56**, 2875 (1997).
55. M. Kortelainen, R.J. Furnstahl, W. Nazarewicz, and M. Stoitsov, Phys. Rev. **C82**, 011304 (2010).
56. H. Mueller and B.D. Serot, Nucl. Phys. **A606**, 508 (1996).
57. C.J. Horowitz and B.D. Serot, Nucl. Phys. **A368**, 503 (1981).
58. B.D. Serot and J.D. Walecka, Adv. Nucl. Phys. **16**, 1 (1986).
59. J. Boguta and A.R. Bodmer, Nucl. Phys. **A292**, 413 (1977).
60. D.H. Youngblood, H.L. Clark, and Y.W. Lui, Phys. Rev. Lett. **82**(4), 691 (1999).
61. Y.W. Lui, D.H. Youngblood, Y. Tokimoto, H.L. Clark, and B. John, Phys. Rev. **C70**, 014307 (2004).
62. M. Uchida *et al.*, Phys. Lett. **B557**, 12 (2003).
63. M. Uchida *et al.*, Phys. Rev. **C69**, 051301 (2004).
64. T. Li *et al.*, Phys. Rev. Lett. **99**, 162503 (2007).
65. T. Li *et al.*, Phys. Rev. **C81**, 034309 (2010).
66. U. Garg and D. Patel; *private communication*.
67. N.K. Glendenning, *Compact Stars* (Springer-Verlag New York, 2000).
68. P. Demorest, T. Pennucci, S. Ransom, M. Roberts, and J. Hessels, Nature **467**, 1081 (2010).
69. J. Antoniadis *et al.*, Science **340**, 6131 (2013).
70. B.G. Todd and J. Piekarewicz, Phys. Rev. **C67**, 044317 (2003).
71. A.L. Fetter and J.D. Walecka, *Quantum Theory of Many Particle Systems* (McGraw-Hill, New York, 1971).
72. W.H. Dickhoff and D. Van Neck, *Many-body Theory Exposed* (World Scientific Publishing Co., 2005).
73. J.F. Dawson and R.J. Furnstahl, Phys. Rev. **C42**, 2009 (1990).
74. J. Piekarewicz, Phys. Rev. **C62**, 051304 (2000).
75. J. Piekarewicz, Phys. Rev. **C64**, 024307 (2001).
76. Z.Y. Ma, A. Wandelt, N. Van Giai, D. Vretenar, P. Ring, and L.G. Cao, Nucl. Phys. **A703**, 222 (2002).
77. G. Audi, A.H. Wapstra, and C. Thibault, Nucl. Phys. **A729**, 337 (2002).
78. J.P. Blaizot, J.F. Berger, J. Dechargé, and M. Girod, Nucl. Phys. **A591**, 435 (1995).
79. J. Piekarewicz, Phys. Rev. **C69**, 041301 (2004).
80. J. Piekarewicz, Phys. Rev. **C66**, 034305 (2002).
81. P.G. Reinhard and W. Nazarewicz, Phys. Rev. **C81**, 051303 (2010).
82. J. Piekarewicz, Phys. Rev. **C83**, 034319 (2011).
83. J. Piekarewicz *et al.*, Phys. Rev. **C85**, 041302(R) (2012).
84. X. Roca-Maza *et al.*, arXiv:1307.4806 [nucl-th] (2013).
85. A. Tamii *et al.*, Phys. Rev. Lett. **107**, 062502 (2011).
86. I. Poltoratska *et al.*, Phys. Rev. **C85**, 041304 (2012).
87. W. Satula, R.A. Wyss, and M. Rafalski, Phys. Rev. **C74**, 011301 (2006).
88. G.A. Lalazissis, J. König, and P. Ring, Phys. Rev. **C55**, 540 (1997).
89. G.A. Lalazissis, S. Raman, and P. Ring, At. Data Nucl. Data Tables **71**, 1 (1999).
90. B.G. Todd-Rutel and J. Piekarewicz, Phys. Rev. Lett **95**, 122501 (2005).
91. A.W. Steiner, J.M. Lattimer, and E.F. Brown, Astrophys. J. **722**, 33 (2010).
92. F.J. Fattoyev, C.J. Horowitz, J. Piekarewicz, and G. Shen, Phys. Rev. **C82**, 055803 (2010).
93. F.J. Fattoyev and J. Piekarewicz, arXiv:1306.6034 [nucl-th] (2013).
94. W.C. Chen, J. Piekarewicz, and M. Centelles, Phys. Rev. C (in press); arXiv:1304.2421 [nucl-th] (2013).
95. J. Piekarewicz, Phys. Rev. **C76**, 031301 (2007).
96. H. Sagawa, S. Yoshida, G.M. Zeng, J.Z. Gu, and X.Z. Zhang, Phys. Rev. **C76**, 034327 (2007).
97. A. Avdeenkov *et al.*, Phys. Rev. **C79**, 034309 (2009).
98. J. Piekarewicz, J. Phys. **G37**, 064038 (2010).
99. L.G. Cao, H. Sagawa, G. Colò, Phys. Rev. **C86**, 054313 (2012).
100. D. Patel *et al.*, Phys. Lett. **B718**, 447 (2012).
101. J. Li, G. Colò, and J. Meng, Phys. Rev. **C78**, 064304 (2008).
102. E. Khan, Phys. Rev. **C80**, 011307 (2009).
103. E. Khan, Phys. Rev. **C80**, 057302 (2009).
104. E. Khan, J. Margueron, G. Colò, K. Hagino, and H. Sagawa, Phys. Rev. **C82**, 024322 (2010).
105. P. Vesely, J. Toivanen, B.G. Carlsson, J. Dobaczewski, N. Michel, and A. Pastore, Phys. Rev. **C86**, 024303 (2012).
106. X. Roca-Maza, G. Colò, and H. Sagawa, Phys. Rev. **C86**, 031306 (2012).
107. Y. Suzuki, K. Ikeda, and H. Sato, Prog. Theor. Phys. **83**, 180 (1990).
108. P. Van Isacker, D.D. Nagarajan, and M.A. Warner, Phys. Rev. **C45**, R13 (1992).
109. I. Hamamoto, H. Sagawa, and X.Z. Zhang, Phys. Rev. **C53**, 765 (1996).
110. I. Hamamoto, H. Sagawa, and X.Z. Zhang, Phys. Rev. **C57**, R1064 (1998).
111. D. Vretenar, N. Paar, P. Ring, and G.A. Lalazissis, Phys. Rev. **C63**, 047301 (2001).
112. D. Vretenar, N. Paar, P. Ring, G.A. Lalazissis, Nucl. Phys. **A692**, 496 (2001).
113. N. Paar, P. Ring, T. Niksic, and D. Vretenar, Phys. Rev. **C67**, 034312 (2003).
114. N. Tsoneva, H. Lenske, and C. Stoyanov, Phys. Lett. **B586**, 213 (2004).
115. D. Sarchi, P.F. Bortignon, and G. Colò, Phys. Lett. **B601**, 27 (2004).
116. N. Paar, T. Niksic, D. Vretenar, and P. Ring, Phys. Lett. **B606**, 288 (2005).
117. J. Piekarewicz, Phys. Rev. **C73**, 044325 (2006).
118. N. Tsoneva and H. Lenske, Phys. Rev. **C77**, 024321 (2008).
119. A. Klimkiewicz *et al.*, Phys. Rev. **C76**, 051603 (2007).
120. P. Adrich *et al.*, Phys. Rev. Lett **95**, 132501 (2005).
121. O. Wieland *et al.*, Phys. Rev. Lett. **102**(9), 092502 (2009).
122. D. Rossi *et al.*, J. Phys. Conf. Ser. **420**, 012072 (2013).
123. D. Savran, T. Aumann, and A. Zilges, Prog. Part. Nucl. Phys. **70**, 210 (2013).
124. Building a universal nuclear energy density functional. URL <http://unedf.org>. (UNEDF Collaboration).
125. M. Kortelainen *et al.*, Phys. Rev. **C82**, 024313 (2010).
126. F.J. Fattoyev and J. Piekarewicz, Phys. Rev. **C84**, 064302 (2011).
127. F.J. Fattoyev and J. Piekarewicz, Phys. Rev. **C88**, 015802 (2012).
128. J. Erler, C.J. Horowitz, W. Nazarewicz, M. Rafalski, and P.G. Reinhard, arXiv:1211.6292 [nucl-th] (2012).